# *Modes of coastal precipitation over southwest India and their relationship to intraseasonal variability*

Article

Published Version

It is advisable to refer to the publisher's version if you intend to cite from the work. See Guidance on citing.

To link to this article DOI: http://dx.doi.org/10.1002/qj.3913

www.reading.ac.uk/centaur

**CentAUR**

Central Archive at the University of Reading

Reading's research outputs online

RESEARCH ARTICLE

# Modes of coastal precipitation over southwest India and their relationship with intraseasonal variability

Kieran M. R. Hunt[1,2] | Andrew G. Turner[1,2] | Thorwald H. M. Stein[1,2] | Jennifer K. Fletcher[3] | Reinhard K. H. Schiemann[1,2]

[1]Department of Meteorology, University of Reading, Reading, UK

[2]National Centre for Atmospheric Science, University of Reading, Reading, UK

[3]School of Earth and Environment, University of Leeds, Leeds, UK

**Correspondence**
K.M.R. Hunt, Department of Meteorology, Whiteknights Campus, University of Reading, Reading, RG6 6BB, UK.
Email: k.m.r.hunt@reading.ac.uk

**Abstract**

The west coast of India, dominated by the Western Ghats mountain range, is among the rainiest places in the Tropics. The interaction between the land–sea contrast of the coast, the monsoonal westerlies, and the oblique mountains is subject to complex intraseasonal variability, which has not previously been explored in depth. This study investigates that variability from the perspective of the land–sea contrast, using empirical orthogonal function analysis to discern regimes of onshore and offshore rainfall over southwest India and the eastern Indian Ocean. Locally, it is found that the rainfall is most sensitive to midtropospheric humidity: when this is anomalously high, deep convection is encouraged; when this is anomalously low, it is suppressed. A moisture-tracking algorithm is employed to determine the primary sources of the anomalously wet and dry midtropospheric air. There are important secondary contributions from low-level vorticity and cross-shore moisture flux. The dominant control on intraseasonal variability in coastal precipitation is found to be the Boreal Summer Intraseasonal Oscillation (BSISO): over 75% of the strongest offshore events occur during phases 3 and 4; and about 40% of the strongest onshore events occur during phases 5 and 6. The location of monsoon low-pressure systems is also shown to be important in determining the magnitude and location of coastal rainfall.

**KEYWORDS**

coastal, convection, India, monsoon, precipitation

## 1 | INTRODUCTION

The west coast of India receives more monsoonal rainfall than any part of monsoonal South Asia except Meghalaya, averaging about three times as much as the rest of the region (Krishnamurthy and Shukla, 2000; Rajeevan *et al.*, 2006). As a result, this region is prone to periods of extremely heavy rainfall (e.g., Venkatesh and Jose, 2007; Deb *et al.*, 2008; Tawde and Singh, 2015; Mishra and Shah, 2018; Hunt and Menon, 2019; Lakshmi *et al.*,

2019; Parchure and Gedam, 2019), which are exaggerated in scale and impact by the presence of the Western Ghats (WGs)—a thin mountain range near the coast, orientated almost perpendicular to the monsoon westerlies. There is thus a pressing need to explore the modes and timescales of variability that drive this rainfall, the understanding of which will improve its predictability. This has been an area of interest to authors for many years, but only recently has the relationship between onshore and offshore precipitation been thought of as an important ingredient in the rainfall variability over the west—and particularly southwest—Indian coastal region (Shige *et al.*, 2017; Fletcher *et al.*, 2018; Zhang and Smith, 2018).

One could reasonably assume that the band of high rainfall along the coast of west India is caused by the forced ascent of moist monsoonal westerlies as they impinge upon the WGs. However, early studies that attempted to model the rainfall this way found that they could not entirely simulate the large-scale pattern or variability seen in observations (e.g., Sarker, 1966). Observations themselves suffered from some uncertainty, due to a relatively sparse gauge network in a relatively mountainous region (Bhowmik and Das, 2007); the precise location of the band of peak rainfall relative to the WGs has only been ascertained with precision in the era of spaceborne precipitation radars (Romatschke and Houze, 2011; Biasutti *et al.*, 2012). Ogino *et al.*, (2016) showed that about a third of all precipitation (i.e., over land and ocean) in the Tropics occurs within 300 km of a coastline, indicating that the land–sea contrast may play an important secondary role in generating precipitation over the western Indian coastline.

There is no doubt among previous studies that the blocking effect of the WGs plays a vital role in triggering nearby precipitation—for example, Tawde and Singh (2015) used gauge data to find that the meridional structure of rainfall followed the orography. However, modelling studies that have removed the WGs have found that rainfall along the west coast does not disappear, but is reduced in intensity by about half (Wu *et al.*, 1999; Xie *et al.*, 2006; Sijikumar *et al.*, 2013), and is less constrained in location—though still parallel to the coastline. These studies also suggest that the lower level monsoonal jet would be stronger in the absence of the WGs, hinting that the blocking might have far-reaching effects across the Arabian Sea. Xie *et al.* (2006) noted that the WGs were the only mountain range in South Asia to retain their associated precipitation band after the orography was flattened, suggesting that, while mountains in the Tropics act as as seeds for convection, the unique location of the WGs plays an equally important role.

Grossman and Durran (1984) used a simple model to show that blocking from the WGs could, through setting up a large-scale pressure gradient, trigger offshore convection under the right conditions (low convective inhibition (CIN) and low lifting condensation level), which might then feed back into the larger monsoonal circulation. Their model did not, however, take latent heating into account; when Ogura and Yoshizaki (1988) included it, they found that such convection happened preferentially over land rather than ocean. Maheskumar *et al.* (2014) found that low-level convergence, wind shear, and convective instability were important precursors for heavy coastal rainfall, additionally noting that convective rainfall was greatly inhibited by advection of dry air into the midtroposphere—a finding in agreement with Grossman and Durran (1984).

There has been some discussion over the nature of this rainfall. Grossman and Garcia (1990) found, using the Highly Reflective Cloud dataset, that the frequency of high cloud over the Arabian Sea and west coast was similar to that over the rest of the subcontinent, implying that deep convection plays a similar role over the region. Later studies refined this as satellite data improved—in particular, with the Tropical Rainfall Measuring Mission (TRMM), finding that the region contained a heterogeneous mix of deep and shallow convection (Maheskumar *et al.*, 2014) and that, while rainfall along the coast was mostly convective, rainfall over the WGs themselves was mostly stratiform (Romatschke and Houze, 2011; Konwar *et al.*, 2014). Romatschke and Houze (2011) analysed the size of contributing convective systems, noting that they were typically small ($<10,000$ km$^2$) or medium ($<44,000$ km$^2$) in size, and finding that such systems were helped considerably in their development by midlevel cyclonic vorticity over the Arabian Sea. Kumar *et al.* (2014) used data from TRMM to show that heavy rainfall events contributed more to the mean rainfall over the WGs and eastern Arabian Sea than anywhere else over the subcontinent, as well as yielding significant cloud ice content and anvil occurrences, suggesting the importance of deep convection; however, they also found a relatively low altitude for the latent heating maximum at 3–4 km. Kumar and Bhat (2017) found that the proportion of shallow clouds was higher over the WGs than anywhere in South Asia, with a modal cloud-top height of about 6 km both onshore and offshore—though a significant proportion of clouds still exceeded 10 km. They found, in agreement with other authors, that a dry midtroposphere limits convection in this region.

More recently, authors have examined potential sources of variability of rainfall over the coastal region. Francis and Gadgil (2006) looked at outgoing long-wave radiation (OLR) data from the *INSAT* satellite and concluded that heavy rainfall along the coast was usually associated with synoptic-scale activity, which they noted had a northward component—consistent with

Boreal Summer Intraseasonal Oscillation (BSISO) forcing (Jiang *et al.*, 2004). The BSISO is often thought of as the northward-propagating branch of the Madden–Julian Oscillation (MJO); however, it extends much farther poleward, having influence as far north as 30°N. It explains about 20% of the intraseasonal variance in five-day mean OLR (Lee *et al.*, 2013) and is usually separated into eight phases; phases 2, 3, and 4 are most commonly associated with enhanced large-scale rainfall over India (Lee *et al.*, 2013, their figure 10). This is also consistent with Hoyos and Webster (2007), who found that the OLR power spectrum had a broad peak between 5 and 50 days, suggesting a complicated temporal structure within, perhaps due to the interaction of intraseasonal variability with the orography, but also implying that more than one large-scale forcing is at work. Shige *et al.* (2017) further highlighted the role of the BSISO, in particular showing that offshore rainfall was preferred during phase 4 and onshore rainfall was preferred during phase 5. Zhang and Smith (2018) identified a case (July 2008) where offshore rainfall transitioned to onshore rainfall; they argued that the former prevents the latter by depleting CAPE and consuming moisture flux. Another transition case (June 2016) was identified by Fletcher *et al.* (2018); they attributed the switch from offshore to onshore rainfall to the northward passage of a nearby low-pressure system in the Bay of Bengal, favourable phases of the BSISO—as per Shige *et al.* (2017)—and the subsequent suppression of deep convection over the Arabian Sea by a midtropospheric dry intrusion.

It is this relationship between onshore and offshore rainfall that interests us the most; so far it has only been the subject of case studies, leading to several important questions being raised by previous studies, in particular Fletcher *et al.* (2018). How common are distinct periods of offshore-only and onshore-only rainfall? Does the former often transition into the latter, or vice versa? What are the differences in atmospheric dynamics, thermodynamics, and moisture between onshore and offshore rainfall? And perhaps most importantly, what role does large-scale intraseasonal variability—such as the BSISO, low-pressure systems, and midtropospheric dry intrusions—play in driving this local variability?

In this article, we will answer these questions: firstly, by using Empirical Orthogonal Function (EOF) analysis to establish an index to quantify the offshore/onshore nature of rainfall over coastal west/southwest India; secondly, by using reanalysis, satellite, and radiosonde data to understand the different atmospheric conditions behind each mode; and, finally, by projecting the relative forcings from different intraseasonal phenomena on to these modes.

We start with a discussion of our methodology and data sources in Section 2, and then discuss the onshore/offshore

metric and its phase space in Section 3. We then cover the composite structure and variability in Section 4, before concluding in Section 5.

## 2 | DATA AND METHODOLOGY

### 2.1 | Data sources

#### 2.1.1 | BSISO and MJO indices

Data for the MJO and BSISO were downloaded from http://iprc.soest.hawaii.edu/users/kazuyosh/Bimodal_ISO.html [Accessed 1st June 2020], the methodology of which is described in Kikuchi and Wang (2010), Kikuchi et al (2012), Kikuchi (2020). These are used to assess the role of large-scale intraseasonal variability in driving coastal rainfall. These datasets both have daily resolution, available from 1979–2017 (MJO) and 1979–2018 (BSISO). Each contains the normalised values of the first two principal components (or RMMs), as well as the resulting phase and amplitude.

#### 2.1.2 | LPS tracks

We use the database of low-pressure system (LPS) tracks from Hunt and Fletcher (2019) in this study. Using six-hourly ERA-Interim data, they tracked LPSs by computing the mean relative vorticity in the 900–800 hPa layer, then performing a spectral truncation at T63 to filter out short-wavelength noise. They then identified positive-definite vorticity regions within this field and determined the centroid location for each one. These centroids were then linked in time, subject to constraints in distance and steering winds, to form candidate LPS tracks. This algorithm has been used for monsoon LPSs by a number of authors (e.g., Martin *et al.*, 2020; Dong *et al.*, 2020; Arulalan *et al.*, 2020). Track data are available at http://gws-access.jasmin.ac.uk/public/incompass/kieran/track_data/lps-tracks_v2.1.2_1979-2019.csv [Accessed 1st June 2020].

#### 2.1.3 | ERA-Interim

For the atmospheric variables used in our analysis, as well as for the fields needed for trajectory analysis, we use the European Centre for Medium-Range Weather Forecasts Interim reanalysis (ERA-I: Dee *et al.*, 2011). All fields are available at six-hourly frequency with a horizontal resolution of T255 (∼78 km at the Equator), distributed over 37 vertical levels spanning from the surface

to 1 hPa. Data are assimilated into the forecasting system from a variety of sources, including satellites, ships, buoys, radiosondes, aircraft, and scatterometers. We do not use variables that are purely model-derived, such as precipitation or cloud cover. ERA-Interim data can be downloaded from https://apps.ecmwf.int/datasets/data/interim-full-daily/levtype=pl/ [Accessed 1st June 2020].

## 2.1.4 | TRMM

Two datasets are used from the Tropical Rainfall Measuring Mission (TRMM: Simpson *et al.*, 1996; Kummerow *et al.*, 1998; 2000). Firstly we use the multi-satellite gridded rainfall product TRMM3B42 (Huffman *et al.*, 1997; 2007; 2010; TRMM, 2011a), available at three-hourly, $0.25° \times 0.25°$ resolution from 1998 onwards. This is used for EOF construction and composite rainfall footprint analysis. We also use data (TRMM2A25) from the 13.8-GHz on-board precipitation radar (Kawanishi *et al.*, 1993; 2000; Iguchi *et al.*, 2000; TRMM, 2011b) to form composite vertical cross-sections of radar reflectivity, which we then use to gauge the vertical extent and intensity of precipitating systems.

## 2.1.5 | CMORPH

CMORPH (Joyce *et al.*, 2004) is also a multisatellite precipitation dataset, though unlike TRMM3B42 it does not undergo a gauge-calibration adjustment process. It is available at hourly, $0.1° \times 0.1°$ resolution from 2000 onwards. We use CMORPH as a high-resolution alternative to TRMM3B42 to replicate results and check the robustness of our findings. Data were downloaded from ftp://ftp.cpc.ncep.noaa.gov/precip/global_CMORPH/3-hourly_025deg/ [Accessed 1st June 2020].

## 2.1.6 | Radiosonde data

Radiosonde data for six stations (Aminidivi, Minicoy, Kochi, Panjim, Mangalore, and Bangalore; see Figure 1) were used in this study. All data were extracted from the University of Wyoming website,[1] where they are freely available. Temporal coverage for each site is given in Figure S1. The data are available at selected pressure levels, which are usually at least every 50 hPa, but vary for each sonde. They are interpolated on to a common vertical axis before analysis.

[1]http://weather.uwyo.edu/upperair/sounding.html [Accessed 1st June 2020]
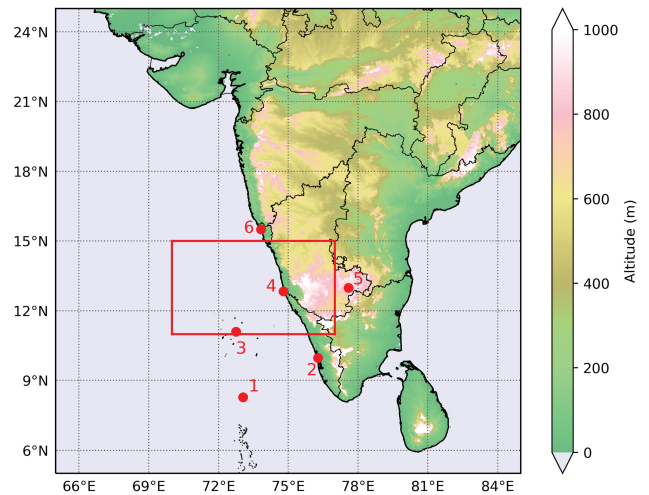


**FIGURE 1** Map showing the orography of south and central India and Sri Lanka. Indian state boundaries are marked in black, the domain used for EOF computation is marked in red. Red dots indicate the locations of nearby radiosonde launch sites, from south to north: 1: Minicoy, 2: Kochi, 3: Aminidivi, 4: Mangalore, 5: Bangalore, 6: Panjim

## 2.2 | Bootstrapping

When we come to look at the role of the BSISO and MJO on principal components of the rainfall (PC1 and PC2), we will test whether the event composite is significantly different from the climatology using a bootstrapping technique as follows.

1. Bin all data points (in our case coordinates defined by principal component analysis) according to the relevant BSISO/MJO phase.
2. Count the number of points in the least populated phase bin. Call this number $N$.
3. Take $N$ randomly chosen pairs of coordinates and find the mean location.
4. Repeat this $10^5$ times, and bin the points by their argument—that is, the angle, $\theta$, that they subtend from the positive abscissa about the origin.
5. For each bin (there are 32 in our case), compute the 95th and 99th percentile radii.
6. Draw the polygons defined by these respective arguments and radii.

## 3 | THE PHASE SPACE

We aim here to produce a robust description of the modes of precipitation over southwest India, in particular following the case study of Fletcher *et al.* (2018). We start by filtering TRMM 3B42 precipitation using a 48-hr low-pass
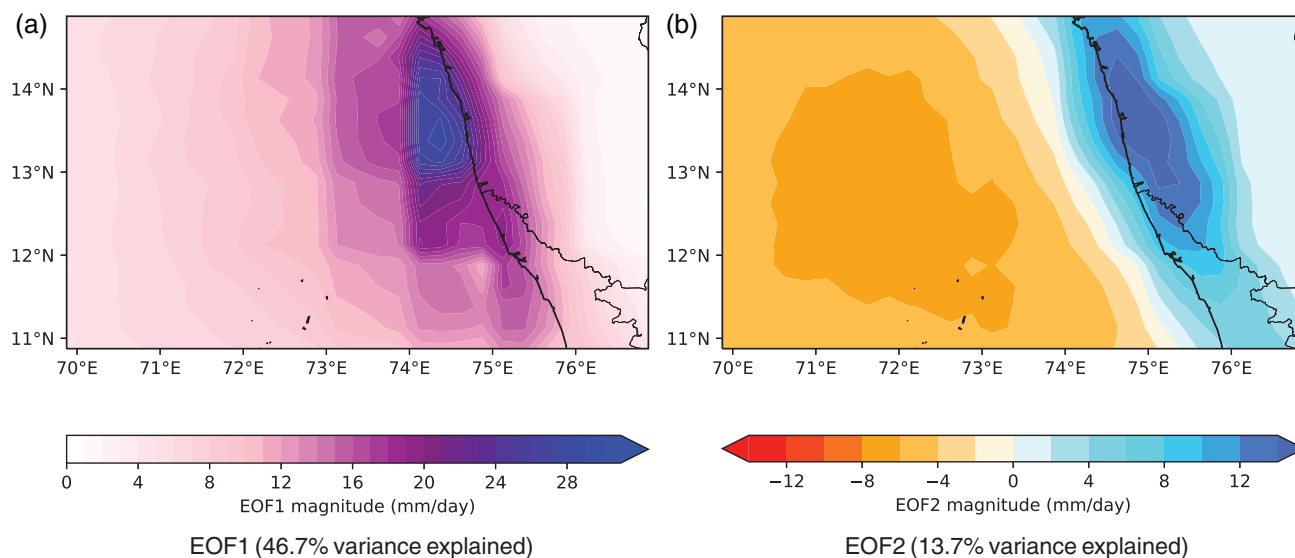
**FIGURE 2**    Spatial patterns of the first two EOFs of coastal rainfall [mm·day⁻¹]. Coastline and Indian state boundaries are marked in black

Lanczos filter (Duchon, 1979) to remove the effects of diurnal variability, in particular from coastal land–sea breezes, which affect the zonal symmetry of rainfall significantly in our region of interest. We then perform an EOF analysis of TRMM 3B42 precipitation using the domain shown by the red box in Figure 1 [11–15°N, 70–77°E]. The first two EOFs, upon which the rest of this study will largely be based, are given in Figure 2. The first EOF (Figure 2a) explains 46.7% of the precipitation variance in this domain. We note that it is both singularly signed and similar in structure to the climatological monsoon rainfall pattern—indeed, the correlation coefficient between the time series of the first principal component, PC1, and domain-mean rainfall is 0.98—so we can conclude that this mode represents whether rainfall in the region is excited or suppressed, that is, it is a mode that describes regional rainfall *magnitude*.

The second EOF (Figure 2b) explains 13.7% of the variance. This has a zonally antisymmetric pattern, which is positive over land and largely negative over the ocean, thus providing a potentially useful metric for determining whether convection is happening preferentially offshore or onshore.[2] If we construct an alternative "antisymmetry" metric by taking the difference between normalised land precipitation and normalised ocean precipitation, we find that the correlation coefficient between this and the second principal component, PC2, is 0.88. Extracting values of

standardised PC2 for the June 2016 case study in Fletcher *et al.* (2018), we find a minimum of −4.1 on June 23 and a maximum of +3.1 on June 28. We conclude, therefore, that this mode represents the sought antisymmetry concisely. In 21% of all time steps, |PC2|> 1, falling to 7% for |PC2|> 2 and 2% for |PC2|> 3. When the rainfall is "excited", that is, PC1>0, these rise to 49%, 18%, and 5%.

We also carried out a sensitivity analysis to determine how robust the onshore–offshore mode (PC2) is against the choice of domain. This was done by varying each of the domain boundaries and tracking the correlation coefficient between the existing and new PC2 time series. The correlation coefficient remained very close to 1 (i.e., greater than 0.8) for extension of the northern boundary until about 17°N, at which point the variance explained diminished and the onshore–offshore mode became the third EOF, though its PC time series retained a high correlation with the original PC2 until 19°N. The southern boundary could be extended until 8.5°N, where the same effect occurred. For the western boundary, the limit was 62.5°E, and for the eastern boundary, 84°E. We can thus be sure that the modes outlined earlier are also representative of a larger domain.

Now, to understand how a change in PC2 affects rainfall over southwest India and the Arabian Sea, we use a Hovmöller-like construction (see Figure 3), where domain rainfall is averaged over latitude and then binned by longitude and PC2. As expected, rainfall is heaviest over the ocean when PC2< − 2 and heaviest over the land when PC2>2, but there are some notable asymmetries. Rainfall associated with negative PC2 covers a much broader area and falls almost exclusively over the ocean, whereas

---

[2] Note that in Fletcher *et al.* (2018) and Zhang and Smith (2018), what we call *onshore* modes are referred to as *coastal* modes. We use the terms interchangeably in this study, but prefer and recommend the former for clarity.
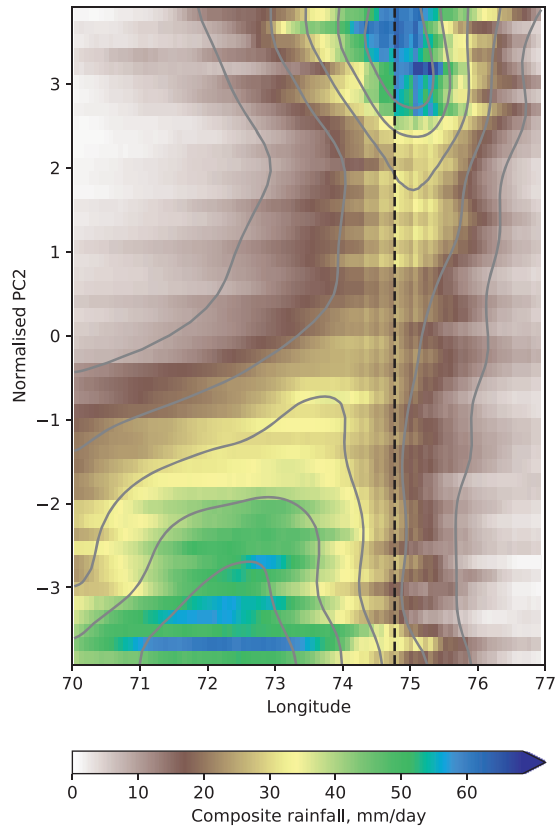
**FIGURE 3** Composite rainfall (from CMORPH) over the domain, averaged over latitude and binned by longitude and PC2 magnitude. Events where rainfall is suppressed, that is, PC1<0, are not included. The black dashed line indicates the location of the coastline at 13°N; grey contours are smoothed isohyets in multiples of 10 mm·day$^{-1}$

rainfall associated with positive PC2 is confined to a small band near the coast and, though the rain is heavier over the land, plenty falls over the ocean as well. Furthermore, the mean rainfall is greatest at each end of the spectrum (i.e., with increasing PC2 magnitude), rather than constant throughout. We will explore the causes of these behaviours later in this article.

# 4 | RESULTS

## 4.1 | Three case studies

We have already alluded to the Fletcher *et al.* (2018) case study—an offshore to onshore transistion that occurred during July 2016—in previous sections, as it provides a canonical example against which to compare our results, but one other period that is of particular interest is the August 2018 Kerala floods (e.g., Mishra and Shah, 2018; Sudheer *et al.*, 2019; Hunt and Menon, 2019), in which sustained rainfall over the WGs resulted in

catastrophic flooding in southwest India. For comparison, we also include the July 2008 transition case identified by Zhang and Smith (2018). Figure 4 shows the phase space described by the first two PCs for all dates, with the trajectories of the June 2016 (case 1), August 2018 (case 2), and July 2008 (case 3) events superimposed in black, blue, and red, respectively.

Case 1 behaves as expected, based on the analysis of Fletcher *et al.* (2018): PC1 is consistently quite positive, indicating generally high rainfall over the domain, whereas PC2 lurches from very negative to very positive on a timescale of about two days. Given the large negative and positive magnitudes of PC2 in this case, it seems reasonable to assume that transitions of such an extent are rather rare. A more detailed investigation reveals that this is the only case during the TRMM period (i.e., since 1998) in which PC2 has gone from −3 to +3 in the space of five days or fewer. That number rises to 4 for −2 to +2 transitions (among them the July 2008 case), and to 32 for −1 to +1 transitions, with the stipulation on each that PC1 does not fall below zero at any point. Interestingly, these numbers fall to 0, 1, and 17 respectively for the reverse transition (i.e., onshore to offshore), indicating a relatively strong preference for transition events from offshore to onshore.

Case 2, the flood case, starts with light onshore rainfall (positive PC2), before a significant intensification of both modes lasting for several days, finishing with a slow return to a no-rainfall state. PC2 exceeded +4 on the morning of August 13, and in doing so created only the seventh such period since the start of the dataset in 1998. It is interesting to note that this event is described so clearly by PC2, given that the majority of rainfall associated with these floods fell outside the EOF domain (compare, e.g., figures 1 and 3 of Hunt and Menon (2019)).

## 4.2 | A composite picture

### 4.2.1 | Reanalysis

We have seen that very different rainfall regimes exist over coastal southwest India, that they can emerge rapidly, and that they can cause significant hydrological stress. We now seek to understand the large-scale drivers that result in such conditions developing. To that end, in this section we will compare the different synoptic conditions behind "strong" onshore and offshore events, that is, those where |PC2|>2. Of the 2,562 days in the TRMM observational record we have used (June–September 1998–2018 inclusive), there is a strong offshore event in 158 of them (6.2%) and a strong onshore event in 117 of them (4.6%). Composite synoptic charts for these events are shown in Figure 5.
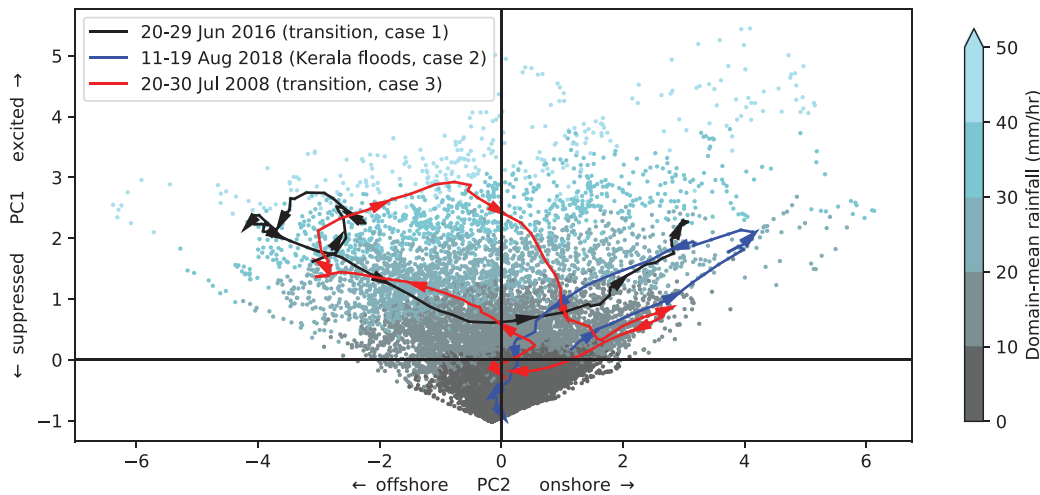
**FIGURE 4**   Phase space of coastal rainfall, with each dot representing a three-hourly datum from TRMM 3B42. The July 2008 transition case from Zhang and Smith (2018), the June 2016 transition case from Fletcher *et al.* (2018), and the 2018 Kerala floods are shown in red, black, and blue, respectively. Arrows indicate the direction of travel at each 0000 UTC

The mean 850-hPa relative vorticity in the offshore composite (Figure 5a) is strikingly different from that in the onshore case (Figure 5b). The latter is consistent with an active monsoon trough, or indeed a low-pressure system, whereas in the former the trough is altogether absent—there is, in fact, a composite ridge in the north-west of India. Vertically integrated moisture flux tells a similar story: in the onshore composite, there is consistently strong onshore flow impinging along the length of the WGs, this also forms part of the larger-scale cyclonic flow wrapped around the trough. The offshore composite shares the strong zonal (and presumably cross-equatorial) flux in the western Arabian Sea, but weakens substantially as it passes through a region of high convergence on the way to south India; there is very little on-to-land transport anywhere over the peninsula. In the offshore case, this moisture flux manifests as a region of heavy rainfall centred several hundred kilometres to the west of the south-west coast, collocated with the region of peak moisture flux convergence; there is very little rainfall anywhere else, except in Bangladesh/northeast India. In the onshore case, very heavy rainfall over the WGs appears to derive from the large zonal moisture flux impacting the orography, but it is not the only rainfall: the active trough provides widespread precipitation to the monsoon core zone and Bay of Bengal. These consistent rainfall patterns and the associated coherent synoptic patterns support the notion that PC2 describes real weather regimes. It is also worth noting the striking similarity between the actual rainfall difference in Figure 6c and the EOF pattern that describes the difference (Figure 2b), as well as the correlation pattern between rainfall and PC2 (not shown).

In summary, the onshore and offshore modes are associated with distinct synoptic-scale conditions: onshore with a strong monsoon trough and well-developed monsoon westerlies, offshore with no trough and weaker, more equatorward westerlies. The enthusiastic reader will have noticed that these conditions seem to resemble those present during either LPS/non-LPS days of the monsoon, or certain phases of the BSISO (Kikuchi *et al.*, 2012). We will discuss this further in Section 4.3.

We can gain further insight into the more localised processes responsible for each mode by looking at composite vertical cross-sections, which are given in Figure 6. Given here are winds (parallel to the cross-sectional plane), equivalent potential temperature, and relative humidity, all from ERA-Interim. Note that the mean structure is in agreement with figure 8a of Shrestha *et al.* (2015).

Compared with the onshore composite, the offshore composite has a region of considerably higher $\theta_e$ in the midtroposphere over much of the Arabian Sea at this latitude. This coincides with a region of deep (modelled) cloud and high humidity over the Arabian Sea in the offshore composite, but relatively stratified high-level cloud and a drier midtroposphere in the onshore case. Both composites share cloudiness and high humidity over the Ghats themselves, though the onshore composite has much stronger vertical wind there, which appears to be coupled to the more extensive zonal flow present in the lower troposphere. As expected, there is relative ascent aloft over land in the onshore composite, and over the ocean in the offshore composite.

Comparing our results with the case-study schematic (figure 15) from Fletcher *et al.* (2018) we see significant agreement: the change in height of the 0 m·s$^{-1}$ isotach, lifting from ~550 hPa in the offshore composite to ~450 hPa in the onshore one; the relative midtropospheric dry intrusion towards the west in the offshore composite;
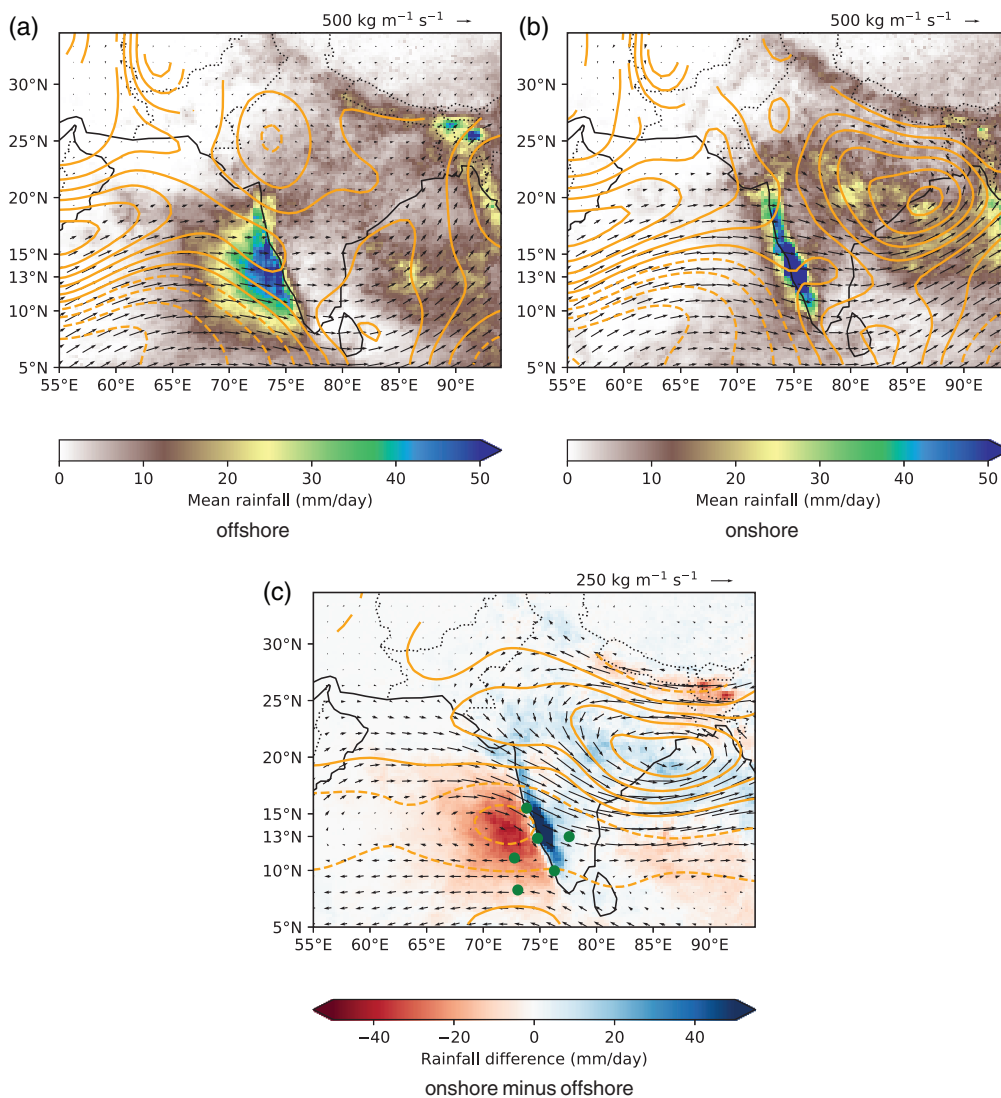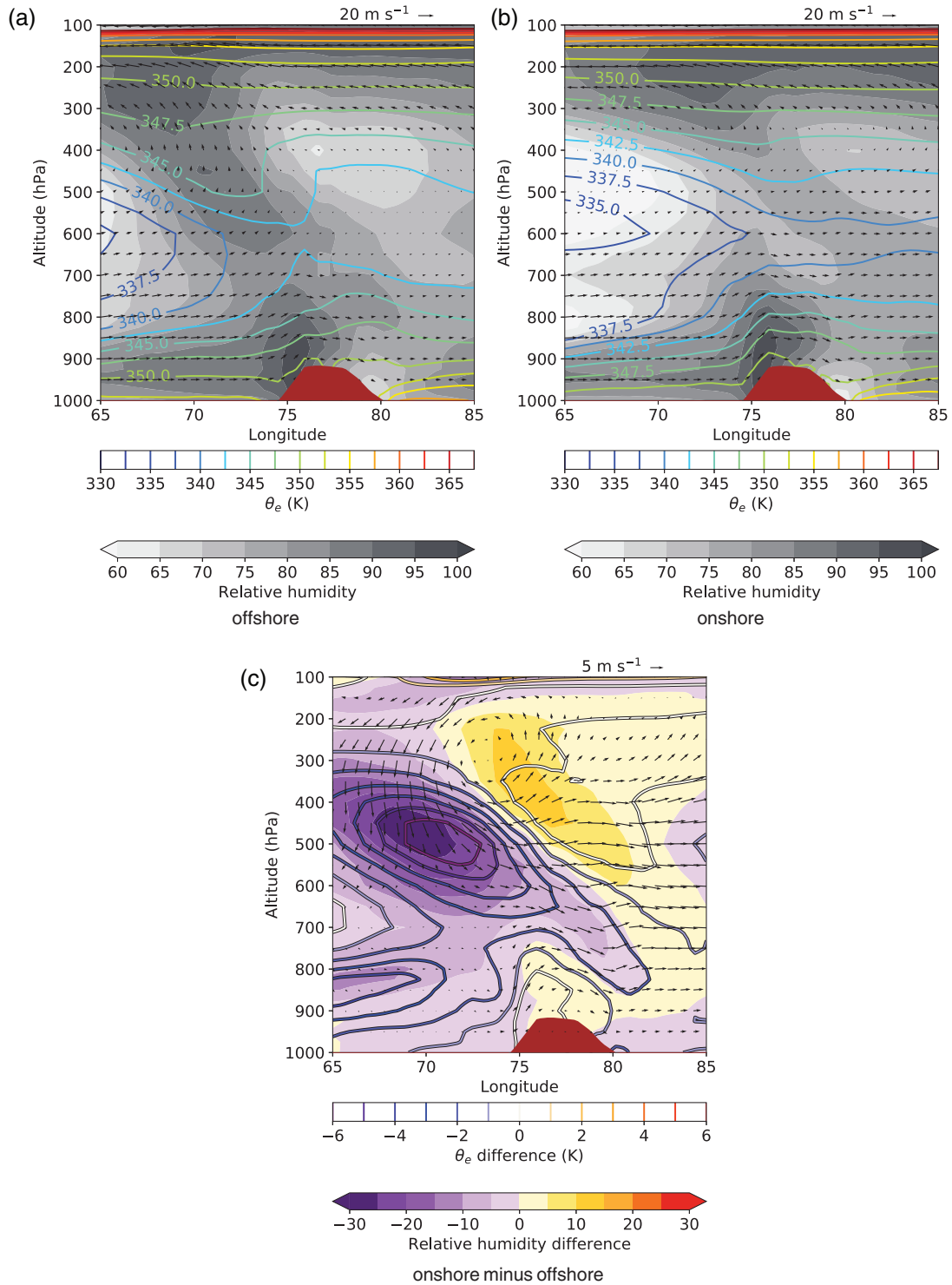
**FIGURE 5** The composite synoptic picture for (a) strong offshore events [PC2< −2], (b) strong onshore events [PC2>2], and (c) their difference. Rainfall values [mm·day$^{-1}$] are shown in solid colours; 850-hPa relative vorticity is shown—where surface pressure is less than 850 hPa—in orange contours at intervals of $5 \times 10^{-6}$ s$^{-1}$, with dashed lines indicating negative values; and vertically integrated moisture flux is given by the quivers, with the scale shown to the top right of each subfigure. Rainfall data are from TRMM 3B42, all other data are from ERA-Interim. Green dots in (c) mark the locations of radiosonde stations used in this study

the comparatively strong onshore flow in the eponymous case; and consistent boundary-layer cloud structure. We note, however, that there are some substantial differences in the overall cloud structure between that schematic and these composites, which may be partially as a result of using a reanalysis product. To remedy this, we now construct composites of radar reflectivity from the TRMM 2A25 product.

### 4.2.2 | Satellite

These satellite-derived composites are shown in Figure 7, which shows frequency, and Figure 8, which shows relative intensity. The average number of scans used to construct a single pixel in the offshore composite is 482, and 388 in the onshore. The microwave imager used for retrieval had a fairly longwave frequency of 13.8 GHz (2.2 cm wavelength) and so, while it could detect

precipitation, it generally could not detect cloud. We see that the offshore composite has wide-scale precipitation over the Arabian Sea—as one would expect—with less common but deeper and more intense convection over the Bay of Bengal. At both coasts there is some encroachment on to land, notably developing into significant convection over the traditional rain shadow of southeast India. In contrast, while the onshore composite has heavy rain focused over the WGs, convection elsewhere is less frequent, shallower, and less intense than in the offshore case. It is particularly interesting to note the difference in scale, alluded to in Figure 5c: the core region (loosely taken as mean echo >10 dBZ) has a zonal width of about 550 km in the offshore composite, but only 95 km in the onshore composite, though the mean echo frequency is much higher in the latter. Previous work has shown that, while storms in the Arabian Sea do tend to have a larger footprint than those over south India (see figure 5b of Hunt and Fletcher, 2019), that does not account for this magnitude of difference,

**FIGURE 6** Cross-section through 13°N of composites of ERA-Interim data for (a) strong offshore events [PC2< −2], (b) strong onshore events [PC2>2], and (c) their difference. Filled contours denote relative humidity [%], line contours denote $\theta_e$ [K], and quivers denote wind parallel to the cross-section plane, with vertical wind exaggerated by a factor of 200

so it is reasonable to conclude that the apparent difference in structure is due to spatial variability in offshore storms. The relative frequency of high-intensity echoes does not vary significantly between offshore and onshore rainfall.

### 4.2.3 | Soundings

We have seen that the difference between onshore and offshore rainfall events appears to involve a relationship between convection and midtropospheric moisture. We
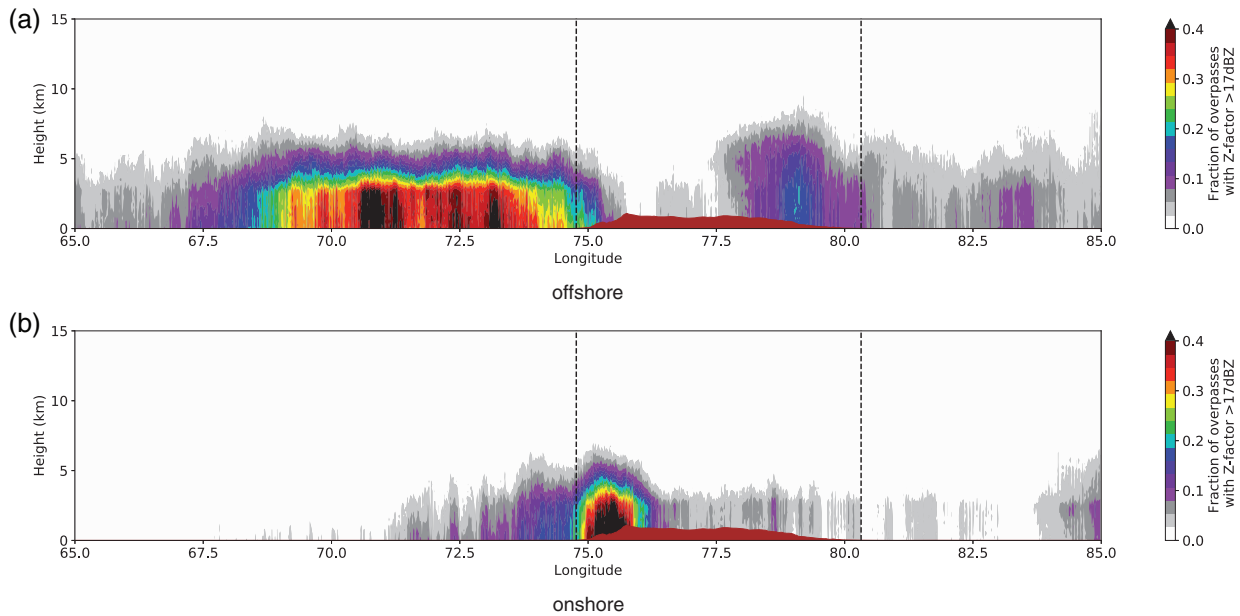
**FIGURE 7**  Fraction of TRMM satellite overpasses (1998–2014) with detectable echoes (reflectivity >17 dBZ) for (a) strong offshore [PC2< − 2] and (b) strong onshore [PC2>2] events. The cross-section is taken through 13°N with a width of 1° (i.e., observations between 12.5°N and 13.5°N are composited). Locations of the Indian coast are given by the dashed black lines and the orography is shown in brown
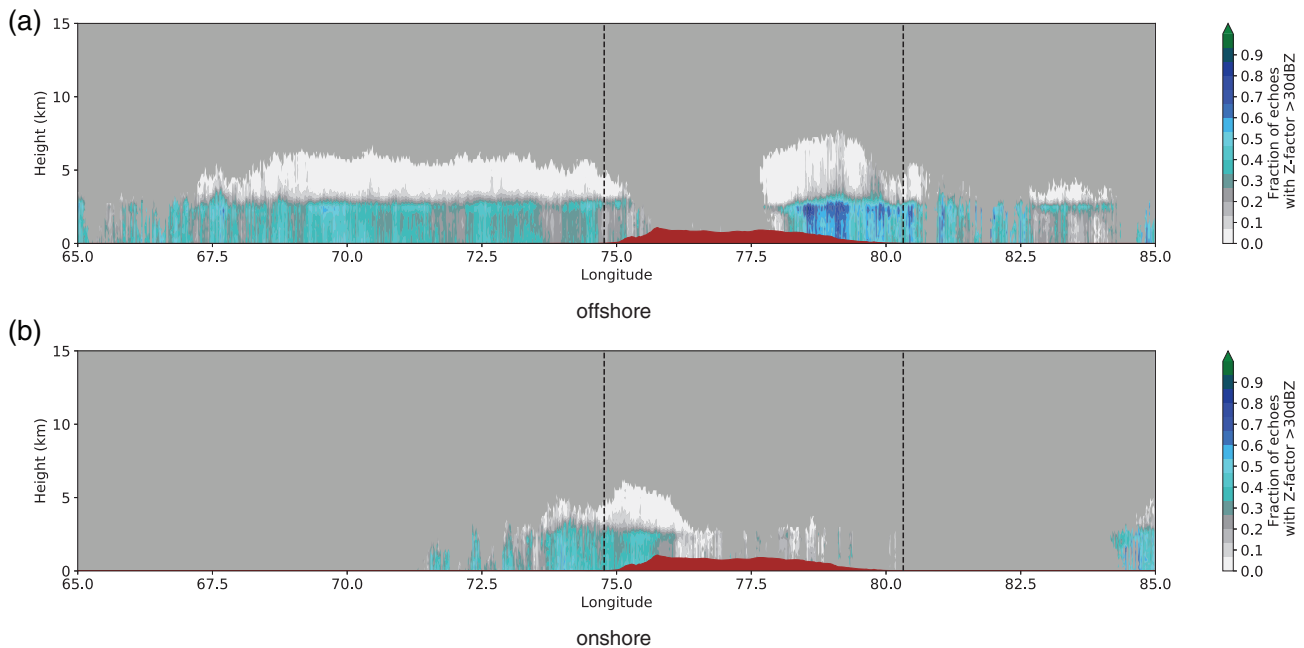


**FIGURE 8**  Fraction of detectable echoes with intense convection (reflectivity >30 dBZ) for (a) strong offshore [PC2< − 2] and (b) strong onshore [PC2>2] events. The cross-section is taken through 13°N with a width of 1° (i.e., observations between 12.5°N and 13.5°N are composited). Locations of the Indian coast are given by the dashed black lines and the orography is shown in brown. Regions are masked in grey where the fraction of overpasses with detectable echoes is less than 0.05

will now employ historic radiosonde data to explore which is the more important driver, or indeed whether one is dependent on the other. There are six radiosonde launch sites of potential interest to us, including two over the

Arabian Sea itself: Aminidivi in the northern Lakshadweep Islands, and Minicoy in the south. Realistically, Minicoy is probably too far south to sample processes in our study region directly (see Figure 5c), but has better data coverage (see Figure S1) and may nonetheless be a useful
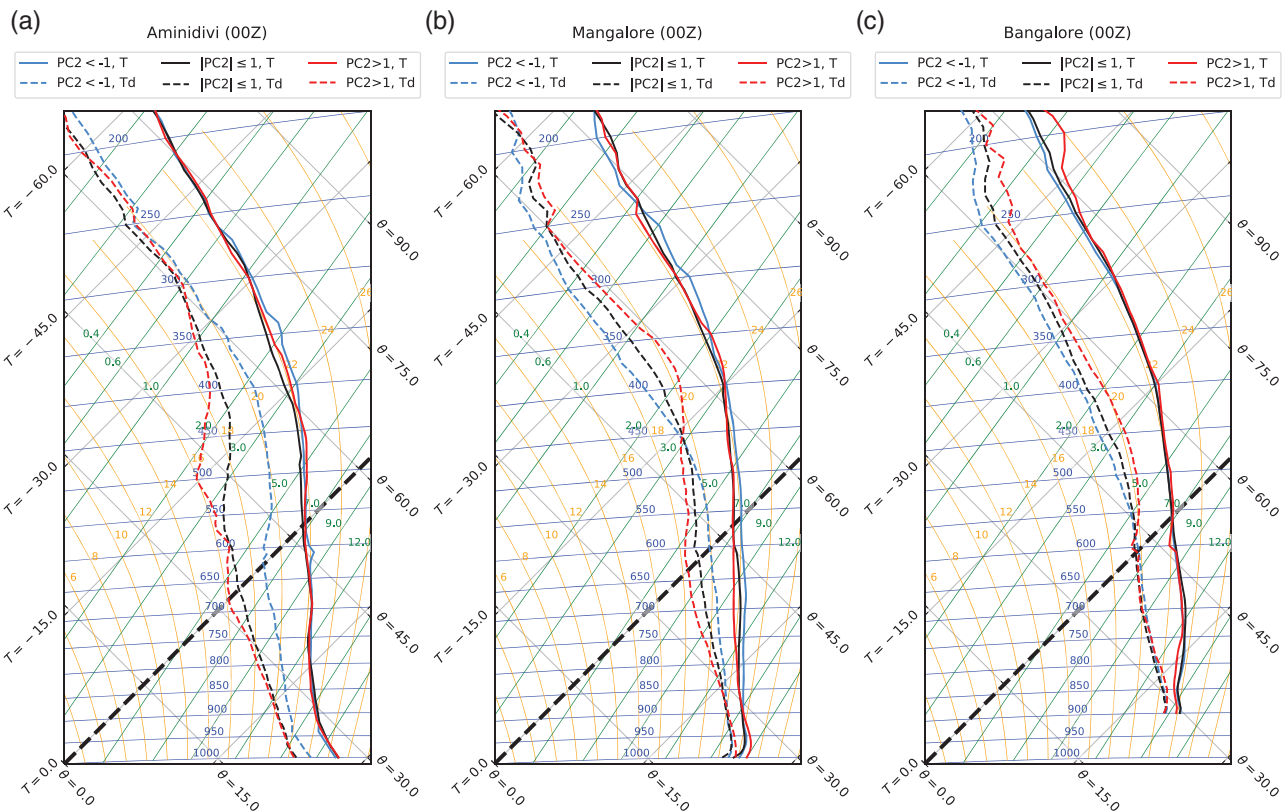
**FIGURE 9** Composite June–September 0000 UTC sounding data for (a) Aminidivi, (b) Mangalore, and (c) Bangalore. Each tephigram is separated into offshore (blue; PC2< − 1), neutral (black; −1≤PC2≤1), and onshore (red; PC2>1) events. Only events with positive PC1 (i.e., active rainfall) are composited.

benchmark. There are four further stations over the peninsula itself. Three lie along the coast, from north to south: Panjim (Goa), Mangalore, and Kochi; one, Bangalore, is inland. Of these, Bangalore and Mangalore lie roughly on the bisecting latitude of the domain (13°N) and are thus of the most use.

Figure 9 shows the mean 0000 UTC soundings for Aminidivi, Mangalore, and Bangalore, separated by rainfall phase. For comparison, the 1200 UTC soundings are provided in Figure S2. Aminidivi (left panel) displays a negligible change in the vertical structure of temperature across the different phases, but there is a significant difference in the midtropospheric humidity. At 0000 UTC, the 500-hPa dewpoint temperature in the offshore composite is −8.5°C, falling to −15.4°C in the onshore composite—corresponding to the relative humidity changing from 78% to 44%. The pattern is similar (although marginally weaker) at 1200 UTC, but the largest difference remains at 500 hPa. The association between a dry midtroposphere off the coast of the WGs and reduced rainfall there was also found by Kumar and Bhat (2017).

Over Mangalore (centre panel), the variation in vertical temperature structure between phases remains slight, but now exceeds 1° in the lower troposphere, as air warmed by

latent heating from the offshore mode is advected over the coast by monsoonal westerlies. Humidity takes on a more complex profile: below 450 hPa, the offshore composite is the most moist; above 450 hPa, the order reverses and the onshore composite becomes the most moist. This pattern can be explained by considering the climatological structure of zonal wind over monsoonal south India: westerlies dominate the lower troposphere, but weaken through 500–400 hPa and become strong easterlies above that layer. Thus the atmospheric column above Mangalore consists of some excess moisture from offshore events advected eastward in the lower levels or some excess moisture from onshore events advected westward in the upper levels (though it may have neither).

Composite soundings for Bangalore (right panel), like the others, have almost no change in temperature between rainfall phases. The strongest signal again comes from humidity, and like Aminidivi it is strongest in the midtroposphere (indeed it is confined to levels above 600 hPa). The largest spread is at about 450 hPa, where the composite mean relative humidity is 62%, 67%, 75% for offshore, neutral, and onshore events, respectively. This reduced variability is at least partially explained by Bangalore being outside the EOF domain and the area

of significantly enhanced precipitation (see Figures 5c and 7b).

To characterise the suitability of the atmosphere for convection during each phase at each station, we compute the mean CAPE and CIN. This is done by computing the variables for each sounding, then taking the composite mean, rather than computing them directly from composite mean soundings. These results, additionally partitioned by sounding time, are given in Figure 10. As we move from maritime to continental regimes (recalling that Minicoy and Aminidivi are in the Arabian Sea; Kochi, Mangalore, and Panjim are on the coast; and Bangalore is inland), we see the expected transition from climatologically high to low values of CAPE, with an increasing impact from the diurnal cycle. Four stations (Minicoy, Aminidivi, Mangalore, Panjim) record an increase in CAPE with increasing PC2, that is, as the phase moves from offshore through neutral to onshore. Only in Aminidivi and Mangalore (those stations within the EOF domain) is this relationship significant, and it is of the wrong sign if we were naively to intuit that changes in CAPE caused the rainfall phases. Mapes and Houze (1992) also noted an anticorrelation between CAPE and rainfall in the Tropics; for southwest India, Fletcher *et al.* (2018) attributed this to boundary-layer humidity being higher during onshore phases. Here, it also appears that sustained latent heating of the upper troposphere during the offshore phase causes the level of neutral buoyancy to subside (this can be seen in the first two panels of Figure 9). The reverse appears to hold for Bangalore. There are no consistent changes in CIN as a function of rainfall phase, despite expected diurnal and land–sea contrast behaviour.

## 4.2.4 | Trajectory analysis

It is clear that midtropospheric humidity plays a crucial role in developing the respective precipitation phases, and that the thermal structure of the atmosphere, at least from the CAPE/CIN point of view, is a feedback, rather than a forcing. The next line of inquiry, therefore, is to determine what process or processes are affecting moisture at the relevant altitudes. To do this, we employ moisture backtrajectory analysis (following that in Hunt *et al.*, 2018). Starting with 500-hPa relative humidity—as that is approximately the level of greatest change between onshore and offshore events, as we saw above—we identify the two $3° \times 3°$ regions where relative humidity changes most between strong onshore and strong offshore events, that is, one for each sign. The largest positive difference between offshore and onshore events occurs over the Arabian Sea, in a box bounded by 68–71°E, 11.5–14.5°N (see Figure 11). The largest positive difference between
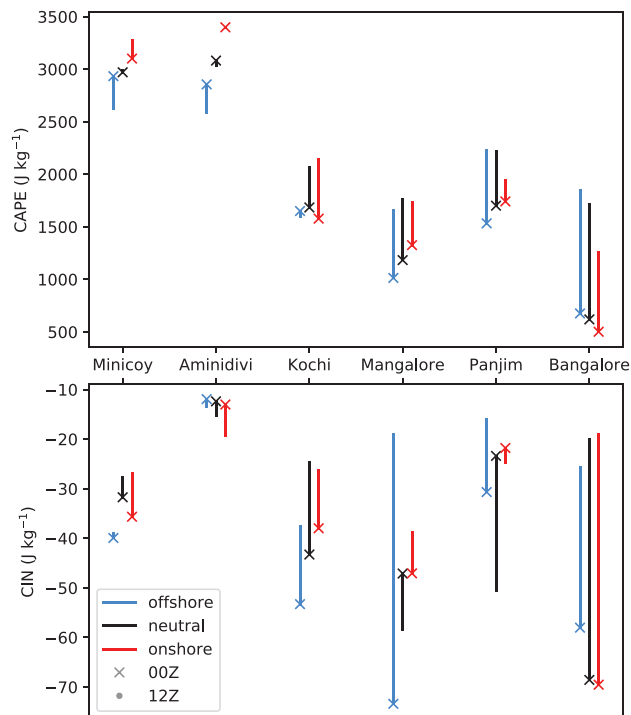


**FIGURE 10** Mean CAPE (top, $J \cdot kg^{-1}$) and CIN (bottom, $J \cdot kg^{-1}$) by sounding site. These are partitioned into offshore (blue), neutral (black), and onshore (red) phases. Mean quantities for 0000 UTC soundings are marked by a cross; a line extends to the 1200 UTC mean

onshore and offshore events occurs over southwest India, in a box bounded by 75–78°E, 12.5–15.5°N (see Figure 12). From each box, we release 36 evenly spaced particles for each of the hundred strongest onshore and offshore events (i.e., 3600 particles per panel in Figures 11 and 12), tracing the trajectories of each through the previous three days. The mean pressure of all trajectories is then projected on to a $0.5° \times 0.5°$ grid. Each panel of these two figures also shows two contours (0.02, 0.1) of the 1° kernel density function, so that we can see from which regions trajectories are more likely to originate. The density function is calculated by dividing the number of trajectories passing through a given $1° \times 1°$ box by the total number of trajectories. Thus the 0.1 contour represents locations where there is a 10% chance of a trajectory passing within 1°.

Figure 11a, therefore, shows the sources of 500-hPa moisture above the hundred strongest offshore events. Moist air enters this region predominantly from the west/southwest, where convective activity has forced large-scale ascent, encouraged by monsoonal westerlies. Some moisture also comes from the north, from the head of the Arabian Sea, but this is very much a secondary contribution. This structure is consistent with the moisture flux composites shown in Figure 5. We know from Figure 9a
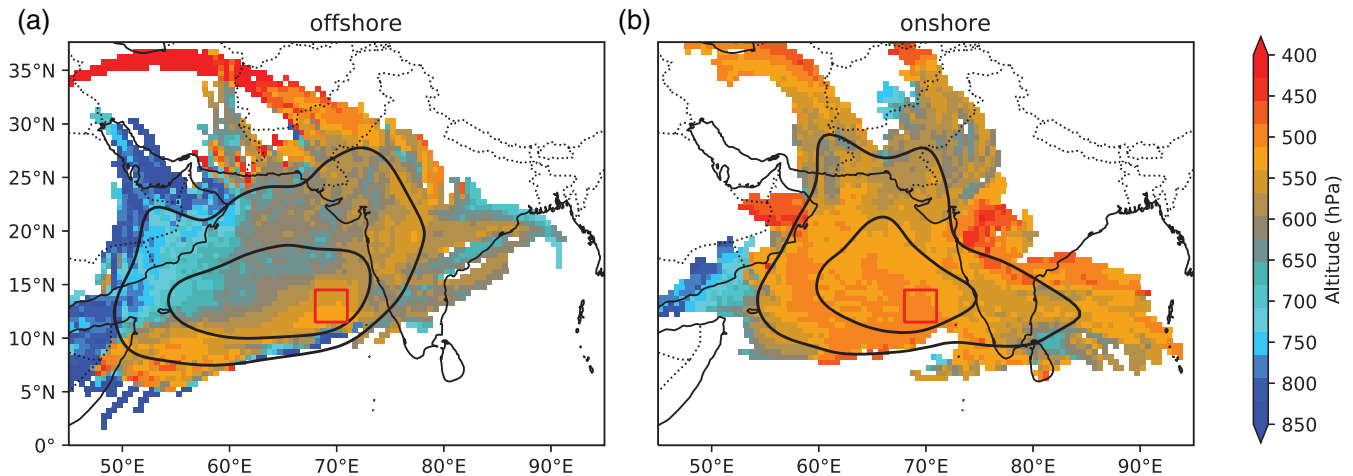
**FIGURE 11**    Mean pressure for backtrajectories originating over the Arabian Sea during (a) the hundred strongest offshore cases (i.e., most negative PC2) and (b) the hundred strongest onshore cases (i.e., most positive PC2). For each case, 36 evenly distributed parcels were released from the red box at 500 hPa and integrated backwards in time through three days. Black contours mark values of 0.02 and 0.1 for the 1° kernel density function
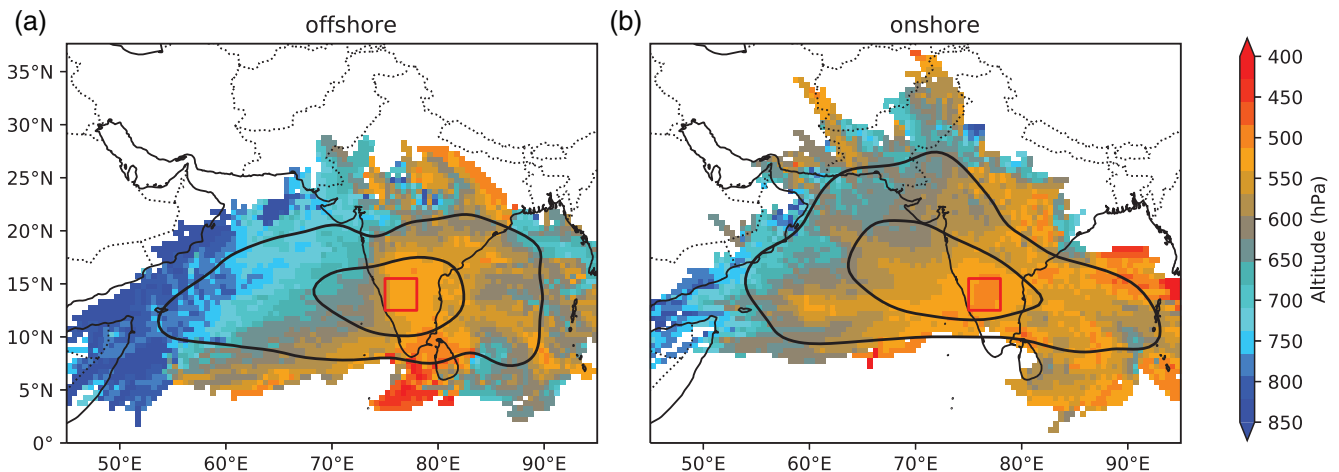


**FIGURE 12**    As Figure 11, but with the release box positioned over southwest India

that the same region has an anomalously dry midtroposphere during onshore events; Figure 11b shows that this air originates mostly from the northern and eastern Arabian Sea and central Asia, but with some additional contributions from over the Indian peninsula itself. The crucial difference here is that the mean pressure of contributing trajectories is midtropospheric, rather than lower-tropospheric; a general lack of large-scale convection in upstream regions deprives these levels of the moisture needed to support deep convection.

Figure 12a shows the origin of land-based midtropospheric parcels during offshore events. At first glance, it is perhaps surprising to see that many of these have an origin in the lower troposphere (to the west), since we expect them to be dry. For the full picture, we need to look at the specific humidity (Figure S4a), which shows that, as

these parcels pass through the active region offshore, they detrain as much as half of their moisture, arriving over the peninsula anomalously dry. For onshore events over this region (Figure 12b), the majority of parcels originate from the northwest, over the head of the Arabian Sea—in agreement with Figure 5c—with a sizeable minority coming from the Bay of Bengal, to the east.

To elucidate these differences further, we consider the behaviour over time of the average trajectory, separated by release box and rainfall phase, in Figure 13. The top panel, showing mean pressure height, shows that, in all cases, the mean parcel ascends before reaching the box. This is perhaps unsurprising, given that the domain on the whole favours convection and large-scale ascent during the monsoon season. Both sets of trajectories released during offshore events originate from lower in the troposphere, but
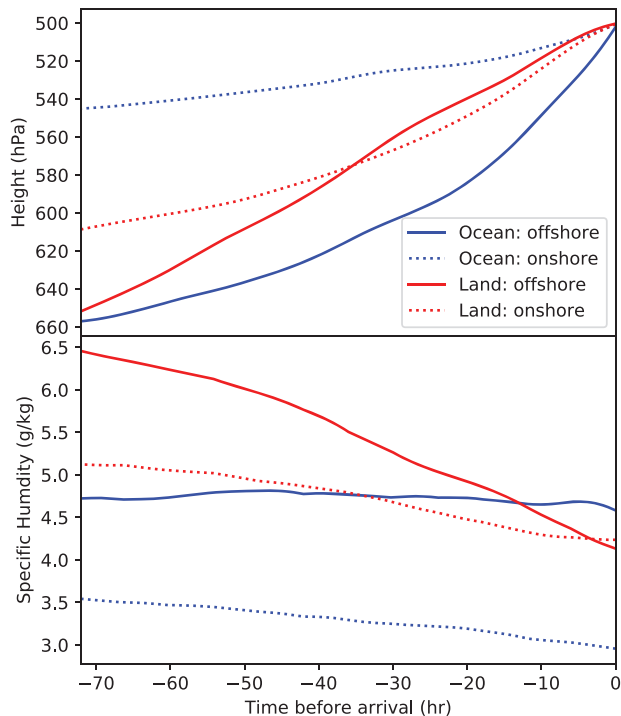
**FIGURE 13** Mean altitude (top) and specific humidity (bottom) of all trajectories considered in Figures 11 and 12, partitioned by release area (blue: ocean, red: land) and phase type (solid: offshore, dotted: onshore)

those ending up over land complete this ascent earlier, giving them time to lose their moisture before reaching their respective box, whereas those that end up over the oceanic box tend to rise mostly in the preceding 24 hours. This is reflected in their mean specific humidities (bottom panel): parcels ending up over land during the offshore phase lose their humidity far more quickly than any of the other categories, presumably as much of it is rained out over the Arabian Sea, in agreement with the results of Zhang and Smith (2018). In contrast, those parcels responsible for the excess midtropospheric moisture over the ocean during offshore phases retain—on average—almost constant specific humidity.

During onshore phases, both sets of parcels undergo less ascent; those over the oceanic box lift through only 40 hPa in the 72 hr prior to the event. Those arriving over the land box are lifted considerably more, about 100 hPa on average, though this is still slightly less than either box during the offshore phase. Both profiles lose moisture at about the same relatively slow rate, with those finishing over the land box starting and finishing moister. This slower drying allows the land parcels to end up very slightly wetter in the onshore cases than the offshore cases, despite starting with about 25% less specific humidity.

To summarise, there is a lot more moisture available during offshore phases, due to increased uplift over the

Arabian Sea. This moistens the midtroposphere above heavy oceanic rainfall, either directly or through detrainment. This process causes significant drying of parcels that eventually make it over land, resulting in a simultaneous period of deficient rainfall there. The reverse is not true during onshore cases, because the lower tropospheric winds in this region are invariably westerly during the monsoon. As such, these events require already dry air to cap or suppress convection over the ocean, allowing moist westerlies to pass through without precipitating their moisture. Together, these explain the subtle asymmetries when comparing the Aminidivi and Bangalore soundings in Figure 9, as well as the crucial role of midtropospheric humidity in controlling these events.

## 4.3 | External forcing

Fletcher *et al.* (2018) hypothesised that the June 2016 transition case was in part driven by the passage of the BSISO. Furthermore, when we inspected other transition cases (Section 4.1), we found that offshore to onshore transitions were far more common than the other way round, indicating that some large-scale forcing may be playing a role. Determing the role of such forcing has important implications for the predictability of these events; in this section, we explore a number of possible controls and assess their capacity to modulate rainfall over southern India.

Figure 14 shows the mean positions of BSISO and MJO phases respectively in the rainfall phase space. For example, the "3" marker in Figure 14a shows the average value of PC1 and PC2[3] when the BSISO is in phase 3. Significance for Figure 14a and Figure 14b is computed by bootstrapping (see Section 2.2); MJO/BSISO phases constructed from randomly sampled subsets of points have 95 and 99% chance of lying within the two concentric circles, respectively.

Phases 3, 4, and 5 of the BSISO are associated with significantly positive values of PC1, indicating that rainfall is excited over southwest India; conversely phases 7, 8, and 1 are associated with suppressed rainfall in the region. This follows from the phase composites given in Kikuchi *et al.* (2012), which show that OLR over south India is at a minimum during phases 3, 4, and 5, and at a maximum during phases 7, 8, and 1. High-resolution composites (Lee *et al.*, 2013; Hsu *et al.*, 2017) also highlight the zonal asymmetry caused by the westward component of the BSISO propagation, which explains why

---

[3]Note that these retain the definition used throughout this article; that is, the first two PCs of southwest rainfall. Where necessary, the principal components of the MJO/BSISO will be preprended with their respective acronym thus: BSISO-PC1.
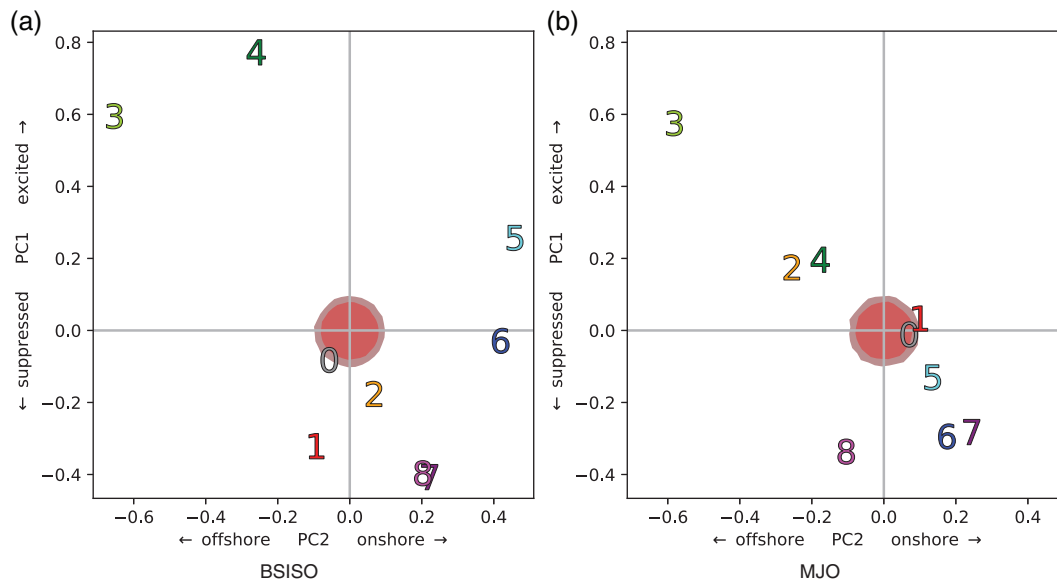
**FIGURE 14** The effect of (a) BSISO and (b) MJO phase on coastal rainfall. For each phase of the BSISO/MJO, the mean location of the coastal rainfall phase is given. Where the standardised amplitude of the BSISO/MJO is less than unity, the phase is taken as zero. The concentric red circles in each figure indicate bootstrap-derived confidence intervals of 95% and 99%, respectively

phases 3 and 4 favour offshore convection and phases 5 and 6 favour onshore convection. Both PC1 and PC2 have a correlation with both BSISO-PC1 and BSISO-PC2 that is significantly different from zero at 99% confidence level. These results are consistent with both Shige *et al.* (2017) and Fletcher *et al.* (2018), who found that phases 4 and 5 of the BSISO were associated with offshore and onshore rainfall respectively, as well as Francis and Gadgil (2006), who found that synoptic-scale variability associated with coastal rainfall often had a northward (i.e., BSISO) component.

In contrast, the MJO (Figure 14b) has less of an influence; in part, this will be due to the BSISO being stronger than the MJO in summer (Kikuchi *et al.*, 2012). Phases 5–8 are associated with suppression of PC1, whereas phases 2, 3, and 4 are associated with its excitation. This is largely in keeping with OLR composites of summer MJO (Wheeler and Hendon, 2004), which indicate that convection is respectively suppressed and favoured during these phases. Despite the eastward propagation of the MJO, there is no clear indication that an excited onshore mode is ever favoured by any particular MJO phase, and it is therefore unlikely that the MJO modulates rainfall over the WGs significantly, even though it can enhance it offshore.

To check the robustness of these relationships, we can reverse the projection—Figure 15 shows the phase spaces for BSISO and MJO in the style of Wheeler and Hendon (2004). For reference, phase 1 of the BSISO is labelled "Equatorial Indian Ocean" and phases increase in the counterclockwise direction; the positioning is the same for the MJO figure. We see that phase 3 is populated most

clearly with offshore events (and phase 5 with onshore), and, though they can happen during any phase, they become increasingly rare as the BSISO moves away from south India. This consolidates results from Figure 14a. The picture for the MJO (Figure 15b) is slightly more cluttered: phases 2, 3, and 4 share most offshore events, with onshore events being more homogeneously distributed. These results are summarised in Table 1.

In summary, the passage of a BSISO event is likely to be associated with offshore convection as it enters phase 3, weakening slightly and becoming onshore convection as it moves through phases 5 and 6. For the MJO, the picture is not quite as well defined, but there is reasonable evidence that phase 3 (and to some extent those either side of it) is associated with offshore convection. Unlike the BSISO, this does not seem to lead to an onshore transition.

We can also examine the role of the monsoon active/break cycle. To do this, we used the definition given by Rajeevan *et al.* (2010)—taking the daily rainfall in July and August averaged over the monsoon core zone, and labelling periods of three or more consecutive days where it is more than one standard deviation over the mean as active (and more than one standard deviation below as break). Projecting our PC1 and PC2 on to these, we find that there is no significant relationship between active/break cycles and PC1, but there is between active/break cycles and PC2. The mean values of PC2 for active, normal, and break conditions are 0.64, −0.02, and −0.26, respectively. This indicates that break conditions favour offshore rainfall slightly and active conditions favour onshore rainfall moderately. The correlation
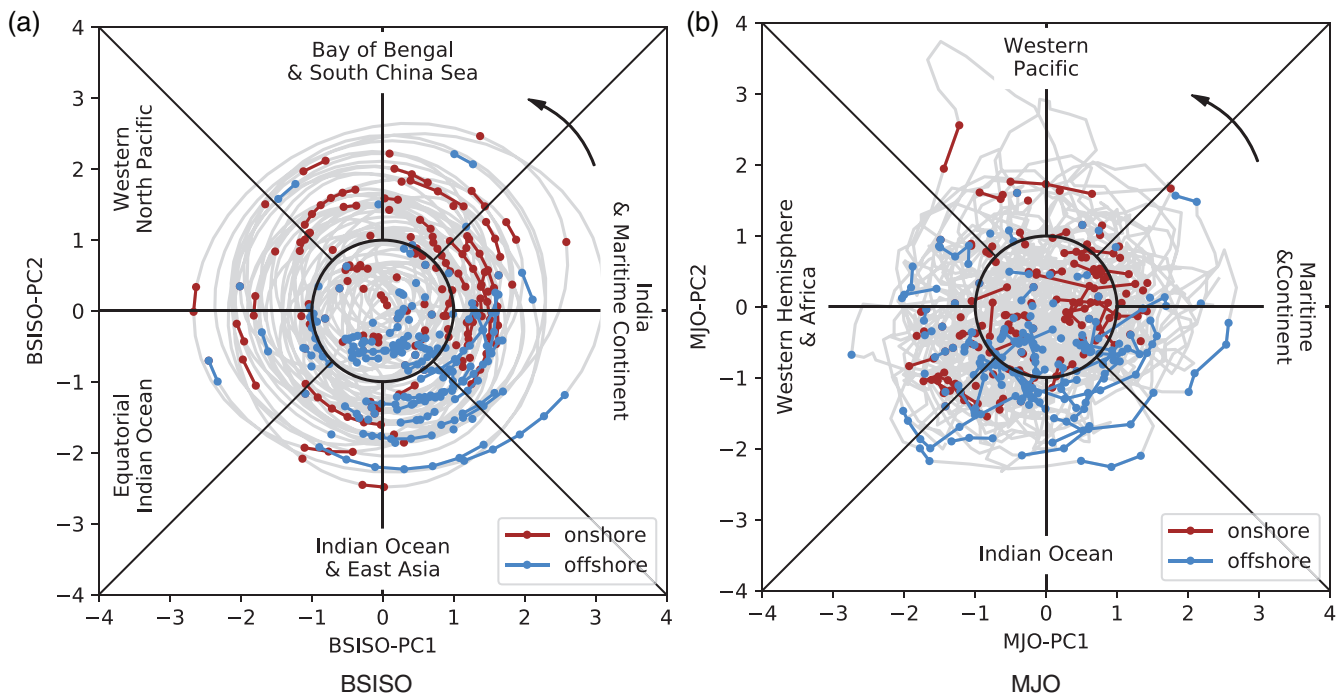
**FIGURE 15** Daily (a) BSISO and (b) MJO phase and amplitude, coloured in blue if that day also had offshore rainfall [PC2< −1], brown if it had onshore rainfall [PC2>1], or grey otherwise. Arrows in the upper left of each subfigure indicate the canonical (counterclockwise) direction of each phenomenon

coefficient for PC2 with a simple active/break metric (i.e., a time series set to −1 for break conditions, +1 for active conditions, and 0 otherwise) is 0.21, which indicates a statistically significant relationship but also that the active/break cycle only explains about 5% of the variance of PC2, less than the BSISO.

Finally, we look at the role of monsoon low-pressure systems (LPSs) in modulating rainfall over southwest India. Such LPSs are responsible for about a quarter of the monsoon rainfall over Kerala (Hunt and Fletcher, 2019) and about a third in Karnataka, the state to the north; we also noted in Figure 5b that the composite synoptic vorticity for strong onshore events resembled an active monsoon trough or LPS. Clearly, the effect of an LPS on PC1 or PC2 is going to be highly sensitive to its location. To represent this, we assign all LPS track points (see Section 2.1.2) into 1° × 1° bins, then calculate the average of PC1 and PC2 when an LPS is in the given bin. The resulting maps, jettisoning all bins with fewer than five tracks, are given in Figure 16.

Interestingly, PC1 (Figure 16a) seems to decrease when there is an LPS in the centre of the monsoon trough region—this implies a fall in rainfall amplitude along the southwestern coastline. A possible explanation is that an LPS in this region will deflect the monsoon westerlies northward, depriving the southwest coastline of some moisture flux. LPSs in the Bay of Bengal have the opposite effect, promoting rain over the coastline, probably through strengthening the westerlies. Those over the Arabian Sea have the strongest effect of all, as these are capable of raining directly over the region, rather than affecting it indirectly through synoptic-scale dynamics. Though typically weaker, cyclonic systems over Sri Lanka also have a strong effect through their reversal of (or destructive interference with) westerlies.

The role of LPSs in driving PC2 (Figure 16b) is a little more subtle. Here, position within the monsoon trough is of considerable importance: an LPS centred along the trough axis is much more likely to be associated with onshore rainfall, whereas those that stray towards the northern or southern boundaries of the trough tend to be associated with offshore rainfall. Those occurring outside the monsoon trough, for example, over Sri Lanka or in the Arabian Sea, have no significant effect, except for a small cluster off the coast of Maharashtra, which deposits rain directly over the offshore region, and is thus strongly associated with a negative PC2.

In conclusion, the choice of LPS "basin" (e.g., monsoon trough, Sri Lanka, Arabian Sea, or Bay of Bengal) is a strong control on PC1, but not on PC2. Location within each basin (particularly the monsoon trough) is a strong control on PC2, but not on PC1.

**TABLE 1** Fraction of offshore and onshore events associated with each phase of the BSISO and MJO, partitioned by intensity

| Phase | Offshore | | | | Onshore | | |
| --- | --- | --- | --- | --- | --- | --- | --- |
| | PC2 < −3 | PC2 < −2 | PC2 < −1 | All | PC2 > 1 | PC2 > 2 | PC2 > 3 |
| BSISO | | | | | | | |
| 0 | 17.2% | 28.9% | 35.9% | 39.2% | 26.2% | 24.4% | 24.2% |
| 1 | 2.3% | 7.7% | 6.9% | 6.9% | 5.0% | 5.4% | 2.1% |
| 2 | 0.0% | 4.0% | 5.7% | 7.8% | 7.3% | 7.9% | 12.6% |
| 3 | **40.7%** | **27.1%** | **25.0%** | 7.9% | 4.6% | 3.1% | 2.1% |
| 4 | **36.2%** | **25.5%** | 18.5% | 8.1% | 11.7% | 8.9% | 8.4% |
| 5 | 0.5% | 4.0% | 3.9% | 7.5% | 16.0% | **22.6%** | **21.6%** |
| 6 | 3.2% | 2.3% | 2.1% | 8.2% | 14.1% | 15.9% | 17.4% |
| 7 | 0.0% | 0.3% | 1.2% | 7.8% | 8.2% | 5.2% | 1.1% |
| 8 | 0.0% | 0.4% | 0.6% | 6.7% | 6.9% | 6.6% | 10.5% |
| MJO | | | | | | | |
| 0 | 36.4% | 27.1% | 31.6% | 46.4% | 46.6% | 48.9% | 44.7% |
| 1 | 11.6% | 1.4% | 6.5% | 11.8% | 15.1% | 15.1% | 17.9% |
| 2 | **21.4%** | 17.2% | **20.7%** | 11.2% | 9.1% | 6.7% | 8.4% |
| 3 | 10.5% | **26.7%** | 17.4% | 3.8% | 1.8% | 1.6% | 1.6% |
| 4 | 8.1% | **22.2%** | 14.1% | 6.0% | 6.5% | 6.4% | 7.9% |
| 5 | 4.1% | 3.2% | 3.7% | 6.8% | 7.5% | 4.1% | 0.0% |
| 6 | 0.8% | 0.0% | 0.4% | 4.2% | 4.4% | 6.6% | 10.5% |
| 7 | 1.7% | 0.0% | 0.0% | 3.9% | 5.5% | 7.0% | 6.3% |
| 8 | 5.3% | 2.3% | 5.7% | 5.8% | 3.5% | 3.6% | 2.6% |

*Note*: Greyed out text indicates phase 0 of the BSISO and MJO, and bold text indicates where the fraction is higher than 20%.

## 4.4 | Spectral analysis

Finally, we turn to the spectral properties of PC1 and PC2, which are shown alongside the other major forcings considered in this work in Figure 17. PC1 and PC2 share a complicated frequency spectrum which peaks between 8 and 20 days and retains power through to at least 50 days (though, given the length of our dataset, we cannot say that this is statistically significant). This broad, complicated spectrum is in agreement with that found to exist in OLR over the coast by Hoyos and Webster (2007). In comparison, LPS spectral power density peaks at about 15 days (with a secondary at about 40), active/break at about 30–40 days (consistent with Rajeevan *et al.*, 2010), and the MJO and BSISO have a broad peak centred at about 40 days.

These results indicate that the onshore–offshore mode of rainfall is probably being modulated by LPS presence and monsoon active/break spells on shorter timescales (i.e., less than 20 days) and by the BSISO/MJO on longer

timescales. However, the complexity of the power spectra shown here and relatively low fractions of variance explained by larger-scale forcing in our earlier analysis strongly suggest that this exists as a physically distinct (if at least partially coupled) mode of variability. We note additionally that there is no statistically significant correlation between PC1 and PC2 at any lag/lead.

## 5 | CONCLUSIONS AND DISCUSSION

Rainfall over southwest India and the eastern Arabian Sea is caused largely by moist monsoonal westerlies striking the WGs orthogonally, and is climatologically some of the heaviest in the Tropics. Yet, despite several case studies, sources of intraseasonal variability in this region have not yet been well constrained. In this study, EOF analysis was applied to 20 years of TRMM rainfall data (using the
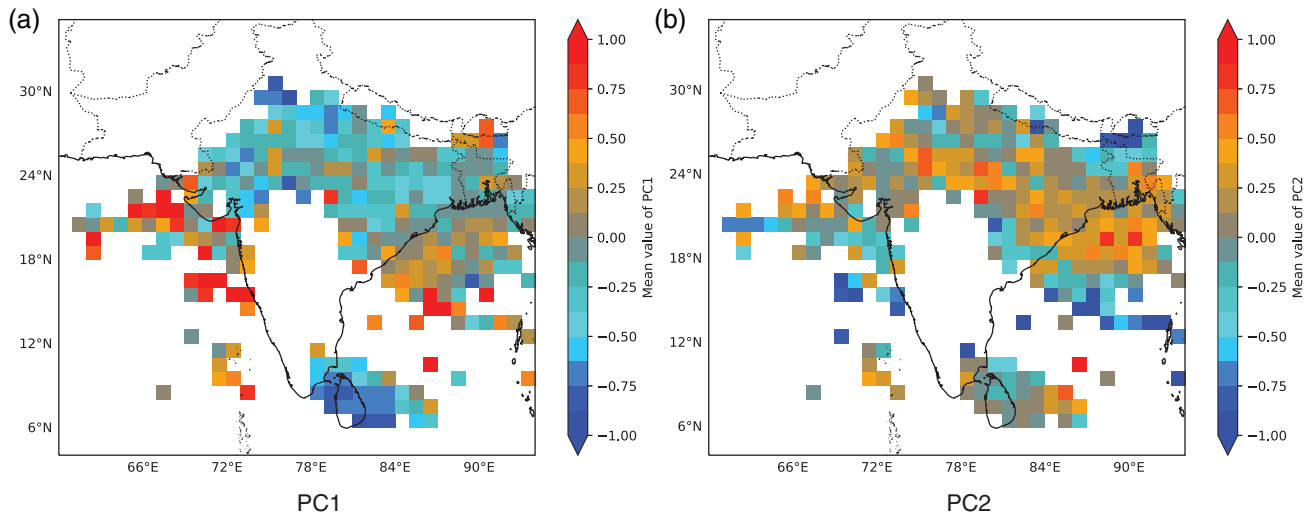
**FIGURE 16** Mean value of (a) PC1 and (b) PC2 when an LPS is present in a given $1° \times 1°$ box. Boxes are coloured white where fewer than five LPS data points are available. Computed for 1998–2016
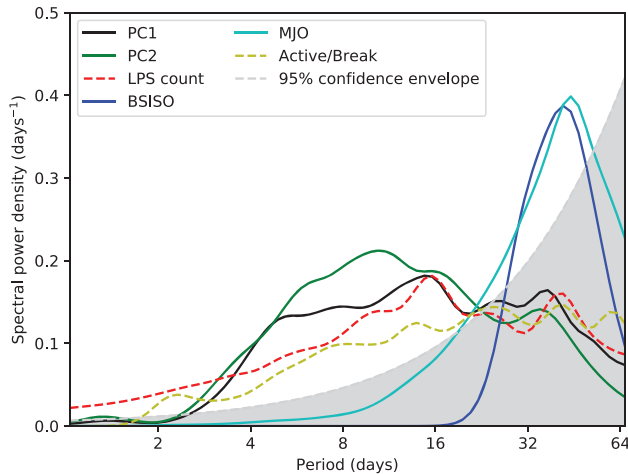


**FIGURE 17** Spectral power density [days$^{-1}$] for PC1 (black), PC2 (green), LPS count (red), BSISO-PC1 (blue), MJO-PC1 (cyan), and monsoon active/break periods (yellow). The 95% confidence envelope is marked in grey. Spectra were computed using a Morlet wavelet transform applied to variance-normalised data

domain 11–15°N, 70–77°E) to derive a metric to quantify whether the rainfall was occurring predominantly offshore (i.e., over the Arabian Sea) or onshore (i.e., along the coast or over the WGs).

The first principal component, PC1, describes the mean rainfall magnitude over the region; the second, PC2, describes the zonal antisymmetry. Negative PC2 implies high rainfall over ocean and low rainfall over land, and positive PC2 implies the opposite. A PC2–PC1 phase diagram was used to characterise cases of offshore→onshore transitions identified in previous studies (Zhang and Smith, 2018; Fletcher *et al.*, 2018), and this shows that the 2018 Kerala floods were an example of a very high PC2

event without preceding offshore rainfall. Transitions like those in the two aforementioned cases were found to be unusual, with most strong onshore (and offshore) events occurring in isolation–only four cases (including those above) in the 20-year record went from PC2< − 2 to PC2>2 within a five-day period. Spectral analysis indicates that both PC1 and PC2 share a broad peak in spectral density between 8 and 20 days.

For the lower troposphere, reanalysis composites showed that onshore cases tended to coexist with a particularly strong monsoon trough, which is generally absent during offshore cases—this modulates the moisture transport, resulting in significantly more northwesterly moisture flux striking the coastline during onshore cases. In contrast, offshore cases are more closely related to local vorticity, in agreement with Romatschke and Houze (2011) and Shige *et al.* (2017). In the midtroposphere, onshore cases are associated with a large region of anomalously low $\theta_e$ over the Arabian Sea, consistent with earlier studies that claimed dry air aloft suppressed offshore convection, allowing additional moisture transport to the coast, in agreement with Maheskumar *et al.* (2014) and Fletcher *et al.* (2018).

TRMM PR satellite composites showed that the precipitating features of onshore cases—where precipitating clouds congregate only along the coastline and mountains—is almost the opposite of that for offshore cases—where clouds congregate in the Arabian Sea, Bay of Bengal, and southeast India. Composite radiosonde data showed that the most important local difference is midtropospheric moisture: the oceanic site, Aminidivi, recorded anomalously high 400-hPa humidity during offshore cases, becoming anomalously low during onshore

cases. The land-based sites of Mangalore and Bangalore recorded the opposite. In contrast to some previous authors, CAPE was not deemed to be an important precursor of precipitation.

Moisture trajectory analysis showed that most anomalously moist midtropospheric air came from large-scale ascent over the north and west Arabian Sea. Anomalously dry midtropospheric air over the land during the offshore phases was found to have also undergone large-scale ascent, but had its moisture removed by either detrainment or precipitation on passing over the offshore region. Anomalously dry midtropospheric air over the Arabian Sea during onshore phases derived largely from northerly dry intrusions.

The role of large-scale forcing on intraseasonal timescales was also examined. It was found, largely in agreement with Shige *et al.* (2017), that phases 3 and 4 of the BSISO were closely associated with offshore rainfall, and phases 5 and 6 were associated (though less closely) with onshore rainfall. The MJO, which typically has low amplitude during the summer monsoon, was associated with offshore rainfall during phase 3, but otherwise had a weak relationship with PC2. LPS location was found to have a strong effect on PC1 (i.e., domain mean rainfall), with presence over the monsoon trough generally weakening rainfall over southwest India and the eastern Arabian Sea, and presence over the Bay of Bengal or Arabian Sea strengthening it. The relationship with PC2 is slightly more nuanced: LPSs positioned along the axis of the monsoon trough are favourable to onshore rainfall, but those too far north or south are favourable to offshore rainfall. The preferential transition from an offshore phase to an onshore phase is consistent with northward propagation of the BSISO, with the reverse transition (onshore to offshore) additionally blocked by a long-trough passage of monsoon LPSs.

In summary, the drivers of onshore and offshore rainfall around southwest India are complex, but midtropospheric humidity is the most important local factor; coupled with lower-tropospheric vorticity over the Arabian Sea and cross-shore moisture flux over land, in agreement with Shige *et al.* (2017). The BSISO and LPS presence are the most important controls on intraseasonal variability.

One important shortcoming of this work was our dependence on TRMM3B42 rainfall data to generate the indices in the first place; strongly vertical wind shear and upper-level easterlies can bias the algorithm into placing precipitation further west in this region than it actually occurred (Shrestha *et al.*, 2015). We also did not examine the seasonal cycle, which may be an important control. We leave this analysis for future work. Another important avenue of future work will be close inspection of strong transition cases—these represent an important

benchmark for modelling, due to their dependence on orography, convection, and large-scale feedbacks.

## ORCID
*Kieran M. R. Hunt* https://orcid.org/0000-0003-1480-3755
*Andrew G. Turner* https://orcid.org/0000-0002-0642-6876
*Thorwald H. M. Stein* https://orcid.org/0000-0002-9215-5397

## REFERENCES
Arulalan, T., AchutaRao, K., Hunt, K.M.R., Turner, A.G., Mitra, A.K. and Sarkar, A. (2020) *Prediction of western disturbances tracks using NEPS*. International Conference on Ensemble Methods in Modelling and Data Assimilation (EMMDA)" 24–26 February 2020. Hosted at NCMRWF, Delhi. URL: Available at: https://www.ncmrwf.gov.in/event/emmda/Abstracts/TArulalan_Abstract_EMMDA.pdf [Accessed 1st June 2020]
Bhowmik, S.K.R. and Das, A.K. (2007) Rainfall analysis for Indian monsoon region using the merged rain gauge observations and satellite estimates: evaluation of monsoon rainfall features. *Journal of Earth System Science*, 116, 187–198.
Biasutti, M., Yuter, S.E., Burleyson, C.D. and Sobel, A.H. (2012) Very high resolution rainfall patterns measured by TRMM precipitation radar: seasonal and diurnal cycles. *Climate Dynamics*, 39, 239–258.
Deb, S.K., Kishtawal, C.M., Pal, P.K. and Joshi, P.C. (2008) Impact of TMI SST on the simulation of a heavy rainfall episode over Mumbai on 26 July 2005. *Monthly Weather Review*, 136, 3714–3741.
Dee, D.P., Uppala, S.M., Simmons, A.J., Berrisford, P., Poli, P., Kobayashi, S., Andrae, U., Balmaseda, M.A., Balsamo, G., Bauer, P., Bechtold, P., Beljaars, A.C.M., van de Berg, L., Bidlot, J., Bormann, N., Delsol, C., Dragani, R., Fuentes, M., Geer, A.J., Haimberger, L., Healy, S.B., Hersbach, H., Hólm, E.V., Isaksen, L., Kållberg, P., Köhler, M., Matricardi, M., McNally, A.P., Monge-Sanz, B.M., Morcrette, J.-J., Park, B.-K., Peubey, C., de Rosnay, P., Tavolato, C., Thépaut, J.-N. and Vitart, F. (2011) The ERA-Interim reanalysis: configuration and performance of the data assimilation system. *Quarterly Journal of the Royal Meteorological Society*, 137, 553–597.
Dong, W.-H., Ming, Y. and Ramaswamy, V. (2020) Projected changes in South Asian monsoon low-pressure systems. *Journal of Climate*. 33, 7275–7287. https://doi.org/10.1175/JCLI-D-20-0168.1.
Duchon, C.E. (1979) Lanczos filtering in one and two dimensions. *Journal of Applied Meteorology and Climatology*, 18, 1016–1022.

Fletcher, J.K., Parker, D.J., Turner, A.G., Menon, A., Martin, G.M., Birch, C.E., Mitra, A.K., Mrudula, G., Hunt, K.M., Taylor, C.M., Houze R.A., Brodzik, S.R. and Bhat, G.S. (2018) The dynamic and thermodynamic structure of the monsoon over southern India: new observations from the INCOMPASS IOP. *Quarterly Journal of the Royal Meteorological Society*, 2867–2890.

Francis, P.A. and Gadgil, S. (2006) Intense rainfall events over the west coast of India. *Meteorology and Atmospheric Physics*, 94, 27–42.

Grossman, R.L. and Durran, D.R. (1984) Interaction of low-level flow with the western Ghat Mountains and offshore convection in the summer monsoon. *Monthly Weather Review*, 112, 652–672.

Grossman, R.L. and Garcia, O. (1990) The distribution of deep convection over ocean and land during the Asian summer monsoon. *Journal of Climate*, 3, 1032–1044.

Hoyos, C.D. and Webster, P.J. (2007) The role of intraseasonal variability in the nature of Asian monsoon precipitation. *Journal of Climate*, 20, 4402–4424.

Hsu, P.-C., Lee, J.-Y., Ha, K.-J. and Tsou, C.-H. (2017) Influences of boreal summer intraseasonal oscillation on heat waves in monsoon Asia. *Journal of Climate*, 30, 7191–7211.

Huffman, G.J., Adler, R.F., Arkin, P., Chang, A., Ferraro, R., Gruber, A., Janowiak, J., McNab, A., Rudolf, B. and Schneider, U. (1997) The global precipitation climatology project (GPCP) combined precipitation dataset. *Bulletin of the American Meteorological Society*, 78, 5–20.

Huffman, G.J., Bolvin, D.T., Nelkin, E.J., Wolff, D.B., Adler, R.F., Gu, G., Hong, Y., Bowman, K.P. and Stocker, E.F. (2007) The TRMM multisatellite precipitation analysis (TMPA): quasi-global, multiyear, combined-sensor precipitation estimates at fine scales. *Journal of Hydrometeorology*, 8, 38–55.

Hunt, K.M.R. and Fletcher, J.K. (2019) The relationship between Indian monsoon rainfall and low-pressure systems. *Climate Dynamics*, 53, 1–13.

Hunt, K.M.R. and Menon, A. (2019) The 2018 Kerala floods: a climate change perspective. *Climate Dynamics*, 54, 2433–2446.

Hunt, K.M.R., Turner, A.G. and Shaffrey, L.C. (2018) Extreme daily rainfall in Pakistan and north India: scale-interactions, mechanisms, and precursors. *Climate Dynamics*, 146, 1005–1022.

Iguchi, T., Kozu, T., Meneghini, R., Awaka, J. and Okamoto, K. (2000) Rain-profiling algorithm for the TRMM precipitation radar. *Journal of Applied Meteorology and Climatology*, 39, 2038–2052. https://doi.org/10.1175/1520-0450(2001)040<2038:RPAFTT> 2.0.CO;2.

Jiang, X., Li, T. and Wang, B. (2004) Structures and mechanisms of the northward propagating boreal summer intraseasonal oscillation. *Journal of Climate*, 17, 1022–1039.

Joyce, R.J., Janowiak, J.E., Arkin, P.A. and Xie, P. (2004) CMORPH: a method that produces global precipitation estimates from passive microwave and infrared data at high spatial and temporal resolution. *Journal of Hydrometeorology*, 5, 487–503.

Kawanishi, T., Kuroiwa, H., Kojima, M., Oikawa, K., Kozu, T., Kumagai, H., Okamoto, K., Okumura, M., Nakatsuka, H. and Nishikawa, K. (2000) TRMM precipitation radar. *Advances in Space Research*, 25, 969–972.

Kawanishi, T., Takamatsu, H., Kozu, T., Okamoto, K. and Kumagai, H. (1993). TRMM precipitation radar. In: *Proceedings of IGARSS '93 - IEEE International Geoscience and Remote Sensing Symposium*, pp. 423–425. Tokyo, Japan: IEEE. https://doi.org/10.1109/IGARSS.1993.322315, (to appear in print).

Kikuchi, K. (2020) Extension of the bimodal intraseasonal oscillation index using JRA-55. *Climate Dynamics*, 54, 919–933, https://doi.org/10.1007/s00382-019-05037-z

Kikuchi, K. and Wang, B. (2010) Formation of tropical cyclones in the northern Indian Ocean associated with two types of tropical intraseasonal oscillation modes. *Journal of Meteorological Society Japan*, 88, 475–496.

Kikuchi, K., Wang, B. and Kajikawa, Y. (2012) Bimodal representation of the tropical intraseasonal oscillation. *Climate Dynamics*, 38, 1989–2000, https://doi.org/10.1007/s00382-011-1159-1.

Konwar, M., Das, S.K., Deshpande, S.M., Chakravarty, K. and Goswami, B.N. (2014) Microphysics of clouds and rain over the Western Ghat. *Journal of Geophysical Research: Atmospheres*, 119, 6140–6159.

Krishnamurthy, V. and Shukla, J. (2000) Intraseasonal and interannual variability of rainfall over India. *Journal of Climate*, 13, 4366–4377.

Kumar, S. and Bhat, G.S. (2017) Vertical structure of orographic precipitating clouds observed over south Asia during summer monsoon season. *Journal of Earth System Science*, 126, 114.

Kumar, S., Hazra, A. and Goswami, B.N. (2014) Role of interaction between dynamics, thermodynamics and cloud microphysics on summer monsoon precipitating clouds over the Myanmar coast and the Western Ghats. *Climate Dynamics*, 43, 911–924.

Kummerow, C., Barnes, W., Kozu, T., Shiue, J. and Simpson, J. (1998) The Tropical Rainfall Measuring Mission (TRMM) sensor package. *Journal of Atmospheric and Oceanic Technology*, 15, 809–817. https://doi.org/10.1175/1520-0426(1998)015<0809:TTRMMT> 2.0.CO;2.

Kummerow, C., Simpson, J., Thiele, O., Barnes, W., Chang, A.T.C., Stocker, E., Adler, R.F., Hou, A., Kakar, R., Wentz, F. Ashcroft, P., Kozu, T., Hong, Y., Okamoto, K., Iguchi, T., Kuroiwa, H., Im, E., Haddad, Z., Huffman, G., Ferrier, B., Olson, W.S., Zipser, E., Smith, E.A., Wilheit, T.T., North, G., Krishnamurti, T. and Nakamura, K. (2000) The status of the Tropical Rainfall Measuring Mission (TRMM) after two years in orbit. *Journal of Applied Meteorology and Climatology*, 39, 1965–1982. https://doi.org/10.1175/1520-0450(2001)040<1965:TSOTTR>2.0.CO;2.

Lakshmi, D.D., Satyanarayana, A.N.V. and Chakraborty, A. (2019) Assessment of heavy precipitation events associated with floods due to strong moisture transport during summer monsoon over India. *Journal of Atmospheric and Solar-Terrestrial Physics*, 189, 123–140.

Lee, J.-Y., Wang, B., Wheeler, M.C., Fu, X., Waliser, D.E. and Kang, I.-S. (2013) Real-time multivariate indices for the boreal summer intraseasonal oscillation over the Asian summer monsoon region. *Climate Dynamics*, 40, 493–509.

Maheskumar, R.S., Narkhedkar, S.G., Morwal, S.B., Padmakumari, B., Kothawale, D.R., Joshi, R.R., Deshpande, C.G., Bhalwankar, R.V. and Kulkarni, J.R. (2014) Mechanism of high rainfall over the Indian west coast region during the monsoon season. *Climate Dynamics*, 43, 1513–1529.

Mapes, B. and Houze, R.A., Jr (1992) An integrated view of the 1987 Australian monsoon and its mesoscale convective systems. I: Horizontal structure. *Quarterly Journal of the Royal Meteorological Society*, 118, 927–963.

Martin, G.M., Brooks, M.E., Johnson, B., Milton, S.F., Webster, S., Jayakumar, A., Mitra, A.K., Rajan, D. and Hunt, K.M.R. (2020) Forecasting the monsoon on daily to seasonal time-scales in

support of a field campaign. *Quarterly Journal of the Meteorological Society*, 146, 2906–2927.

Mishra, V. and Shah, H.L. (2018) Hydroclimatological perspective of the Kerala flood of 2018. *Journal of the Geological Society of India*, 92, 645–650.

Ogino, S.-Y., Yamanaka, M.D., Mori, S. and Matsumoto, J. (2016) How much is the precipitation amount over the tropical coastal region? *Journal of Climate*, 29, 1231–1236.

Ogura, Y. and Yoshizaki, M. (1988) Numerical study of orographic–convective precipitation over the eastern Arabian Sea and the Ghat Mountains during the summer monsoon. *Journal of the Atmospheric Sciences*, 45, 2097–2122.

Parchure, A.S. and Gedam, S.K. (2019) Probability distribution analysis of extreme rainfall events in a flood-prone region of Mumbai, India. *Arabian Journal of Geosciences*, 12, 369.

Rajeevan, M., Bhate, J., Kale, J.D. and Lal, B. (2006) Development of a high resolution daily gridded rainfall data for the Indian region. *Meteorological Monographs*, 91, 296–306. Availble at: https://squall.met.fsu.edu/LAU/070108_1446/doc/ref_report.pdf.pdf [Accessed 1st June 2020].

Rajeevan, M., Gadgil, S. and Bhate, J. (2010) Active and break spells of the Indian summer monsoon. *Journal of Earth System Science*, 119, 229–247.

Romatschke, U. and Houze, R.A., Jr (2011) Characteristics of precipitating convective systems in the south Asian monsoon. *Journal of Hydrometeorology*, 12, 3–26.

Sarker, R.P. (1966) A dynamical model of orographic rainfall. *Monthly Weather Review*, 94, 555–572.

Shige, S., Nakano, Y. and Yamamoto, M.K. (2017) Role of orography, diurnal cycle, and intraseasonal oscillation in summer monsoon rainfall over the Western Ghats and Myanmar Coast. *Journal of Climate*, 30, 9365–9381.

Shrestha, D., Deshar, R. and Nakamura, K. (2015) Characteristics of summer precipitation around the Western Ghats and the Myanmar West Coast. *International Journal of Atmospheric Sciences*, 2015, 206016, https://doi.org/10.1155/2015/206016.

Sijikumar, S., John, L. and Manjusha, K. (2013) Sensitivity study on the role of Western Ghats in simulating the Asian summer monsoon characteristics. *Meteorology and Atmospheric Physics*, 120, 53–60.

Simpson, J., Kummerow, C., Tao, W.-K. and Adler, R.F. (1996) On the Tropical Rainfall Measuring Mission (TRMM). *Meteorology and Atmospheric Physics*, 60, 19–36. https://doi.org/10.1007/BF01029783.

Sudheer, K.P., Bhallamudi, S.M., Narasimhan, B., Thomas, J., Bindhu, V., Vema, V. and Kurian, C. (2019) Role of dams on the floods of August 2018 in Periyar River Basin, Kerala. *Current Science*, 116, 780–794.

Tawde, S.A. and Singh, C. (2015) Investigation of orographic features influencing spatial distribution of rainfall over the Western Ghats of India using satellite data. *International Journal of Climatology*, 35, 2280–2293.

Tropical Rainfall Measuring Mission (TRMM) (2011a), TRMM (TMPA) Rainfall Estimate L3 3 hour 0.25 degree x 0.25 degree V7, Greenbelt, MD, Goddard Earth Sciences Data and Information Services Center (GES DISC), [Accessed 1st June 2020]. https://doi.org/10.5067/TRMM/TMPA/3H/7.

Tropical Rainfall Measuring Mission (TRMM) (2011b), TRMM Precipitation Radar Rainfall Rate and Profile L2 1.5 hours V7, Greenbelt, MD, Goddard Earth Sciences Data and Information Services Center (GES DISC). Available at: https://disc.gsfc.nasa.gov/datacollection/TRMM_2A25_7.html [Accessed 1st June 2020].

Venkatesh, B. and Jose, M.K. (2007) Identification of homogeneous rainfall regimes in parts of Western Ghats region of Karnataka. *Journal of Earth System Science*, 116, 321–329.

Wheeler, M.C. and Hendon, H.H. (2004) An all-season real-time multivariate MJO index: development of an index for monitoring and prediction. *Monthly Weather Review*, 132, 1917–1932.

Wu, Y.-H., Raman, S. and Mohanty, U.C. (1999) Numerical investigation of the Somali jet interaction with the Western Ghat Mountains. *Pure and Applied Geophysics*, 154, 365–396.

Xie, S.-P., Xu, H., Saji, N., Wang, Y. and Liu, W.T. (2006) Role of narrow mountains in large-scale organization of Asian monsoon convection. *Journal of Climate*, 19, 3420–3429.

Zhang, G. and Smith, R.B. (2018) Numerical study of physical processes controlling summer precipitation over the Western Ghats region. *Journal of Climate*, 31, 3099–3115.